Journal of Nuclear Materials 625 (2026) 156520

Contents lists available at ScienceDirect

Journal of Nuclear Materials

journal homepage: www.elsevier.com/locate/jnucmat

Oxidation and degradation of Cr-coated Zr-based alloy up to 1500°C: Effect of Cr thickness

Martin Steinbrueck *, Injae Lee, Ulrike Stegmaier, Chongchong Tang, Michael Stueber

Karlsruhe Institute of Technology, Karlsruhe, Germany

GRAPHICAL ABSTRACT

Calculated mass gain (based on thickness of Cr_2O_3, ZrO_2 and α-Zr(O) layers) depending on temperature and Cr thickness with uncoated Zry-4 as reference. Test durations were 2 hours at 1000 °C, 1 hour at 1200 °C, 30 min at 1300 °C and 10 min at 1400 °C.

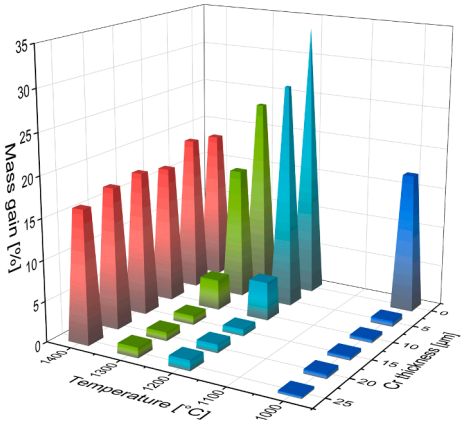

ARTICLE INFO

Keywords:
ATF cladding
Cr coating
Coating thickness
Degradation
High-temperature oxidation

ABSTRACT

This study systematically investigates the influence of chromium coating thickness (5–25 μm) on the oxidation and degradation behavior of Cr-coated Zircaloy-4 under high-temperature steam conditions up to 1500 °C. Using thermogravimetry, hydrogen release monitoring, and extensive post-test microstructural analyses, the results show that thicker Cr coatings significantly extend the protective effect below the Zr–Cr eutectic temperature (~1330 °C). The degradation processes are governed by different diffusion mechanisms that gradually lead to a loss of coating protectiveness, with transition times strongly dependent on coating thickness and temperature. Above the eutectic point, however, all coatings fail almost instantaneously, regardless of thickness, with the oxidation kinetics switching from chromia to zirconia formation. The findings confirm the effectiveness of Cr coatings under normal operation, transients, and design-basis accidents, but demonstrate their intrinsic limitations in beyond-design-basis accident scenarios exceeding the eutectic temperature.

* Corresponding author.
E-mail address: martin.steinbrueck@kit.edu (M. Steinbrueck).

https://doi.org/10.1016/j.jnucmat.2026.156520
Received 30 October 2025; Received in revised form 9 January 2026; Accepted 8 February 2026
Available online 9 February 2026

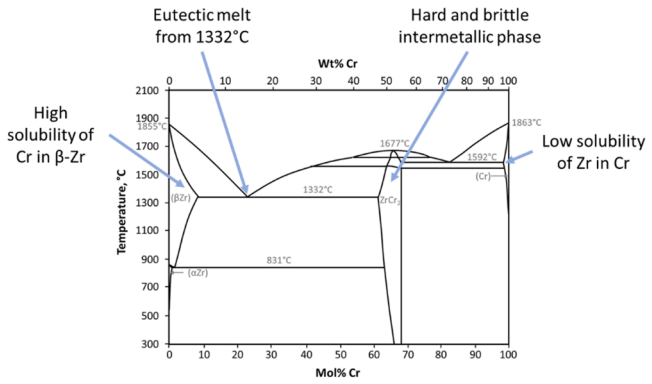

Fig. 1. Binary phase diagram zirconium-chromium (adapted from [20]) and its implications on Cr coating degradation. The data for the pseudo-binary Zry-4-Cr diagram could be slightly affected by the presence of alloying elements in Zircaloy-4 (Sn, O, Fe, Cr).

Table 1
Cr thickness of as-coated samples.

Nominal Cr thickness, μm	Cr thickness side 1, μm	Cr thickness side 2, μm
5	6.05 ± 0.15	5.41 ± 0.11
10	10.35 ± 0.32	10.51 ± 0.40
15	17.70 ± 0.16	17.84 ± 0.27
20	23.26 ± 0.22	23.19 ± 0.20
25	24.38 ± 0.95	24.29 ± 1.00

1. Introduction

The global search for ATF materials for light water reactors (LWRs) began after the nuclear accidents at the Fukushima Daiichi plants, which culminated in hydrogen detonations in three of the four most affected units [1–6]. A major source of hydrogen during a severe nuclear accident is the highly exothermic reaction of zirconium, used for fuel cladding and other structural components, with water vapor. Therefore, the objectives for the development of ATF cladding are (1) to reduce the release of hydrogen and heat, (2) to maintain the mechanical integrity of the cladding as a barrier against the release of radioactive fission products (FP), and thus (3) to gain "coping time" for accident management measures (AMM).

Chromium-coated zirconium-based alloys are the most promising and mature solution for Accident Tolerant Fuel (ATF) cladding [7,8]. The application of a thin coating, typically 10–20 μm thick, requires only minor technological and licensing changes to existing nuclear reactors, making it a near-term solution for ATF cladding. Cr-coated cladding is being developed commercially by Framatome [9] and Westinghouse [10], among others. Lead test rods (LTR) and even full lead test assemblies (LTA) have been tested in commercial pressurized water reactors (PWR) with promising results [11].

The oxidation and degradation mechanisms of Cr coatings have been comprehensively investigated in recent years [12–19]. Oxidation of the metallic chromium coating results in the formation of a well adherent and protective chromia (Cr_2O_3) scale. As long as the coating remains

Table 2
Test matrix and main parameters.

Facility	Temperature	Time/rate	H_2O partial pressure
TG	1000 °C	2 h	1 atm
TG	1200 °C	1h	1 atm
BOX	1300 °C	30 min	0.55 atm
BOX	1400 °C	10 min	0.55 atm
BOX	500–1500 °C	10 K/min	0.55 atm

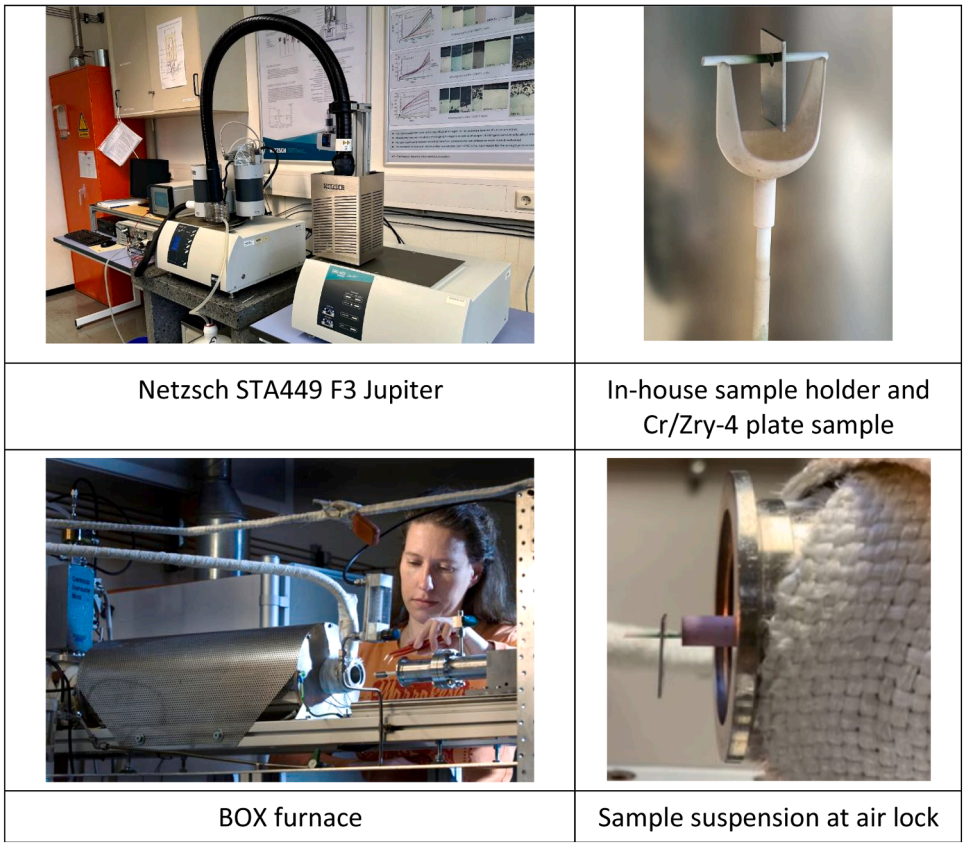

Fig. 2. Test facilities and sample positions.

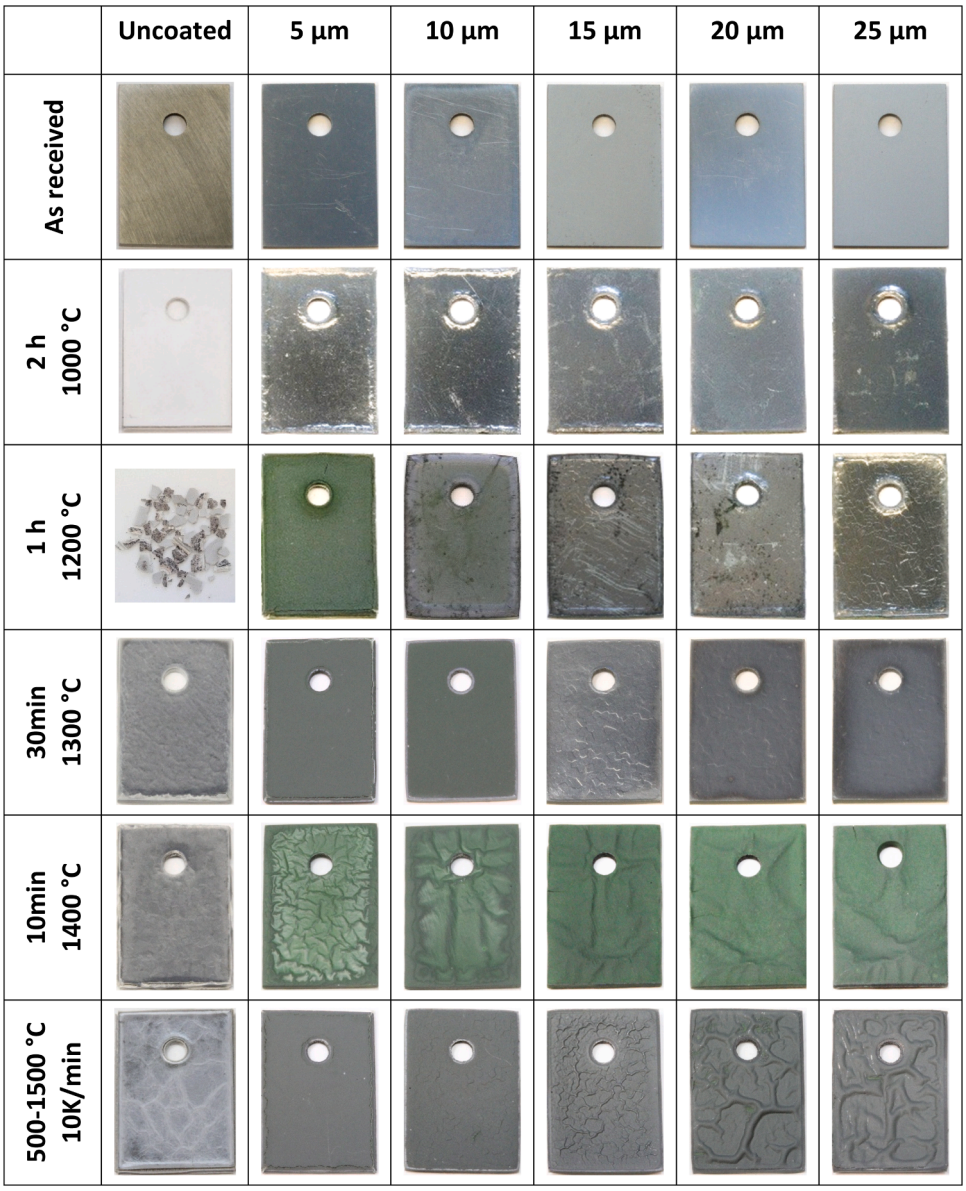

Fig. 3. Post-test appearance of all samples.

protective, the following four-layer sequence is observed: $Cr_2O_3/Cr/ZrCr_2/Zry$. The thin intermetallic $ZrCr_2$ phase layer is formed according to the Zr-Cr phase diagram, which also shows a high solubility of Cr in the high-temperature β-Zr phase, Fig. 1 [20]. This results in diffusion of Cr into the Zr alloy (Zry) bulk at high temperatures, and hence further consumption of the metallic Cr layer. Interestingly, both the oxidation of Cr and the diffusion of Cr into Zry have very similar kinetics despite their different mechanisms as recently demonstrated by Brachet [21]. The degradation of the protective four-layer structure is determined by the diffusion of Zr along Cr grain boundaries (GBs) and its subsequent oxidation to ZrO_{2-x}, which acts as a short-circuit oxygen diffusion path through the metallic Cr once it is throughgoing [14,18]. Later in the high-temperature oxidation/degradation, the Zr/Cr_2O_3 redox reaction takes place, causing the counterintuitive effect of growing Cr and reducing chromia layer thicknesses [18,22]. Furthermore, the oxidation of the $ZrCr_2$ interlayer takes place. In summary, the oxidation of Cr as well as various diffusion processes cause a slow transition from protective to non-protective behavior at high temperatures, which occurs earlier as temperatures rise. For example, at 1200 °C, this transition is observed as a change of parabolic to accelerated kinetics within 30 min and 3 hours depending on the Cr thickness and structure [18,23,24].

However, the most serious feature of the Zr-Cr phase diagram is the eutectic point of around 1330 °C, which results in the rapid formation of a Zr-Cr melt. Once the temperature surpasses this threshold, the protective coating's effectiveness is instantly lost, and the oxidation kinetics shift from chromia formation to zirconia formation. Very high oxidation rates have been observed temporarily in transient tests at around 1330 °C, accompanied by the release of a large amount of hydrogen and chemical heat [19,23]. This occurs because the Zr cladding is exposed to high-temperature oxidation without protection before a protective ZrO_2 layer can form.

In summary, Cr coatings only function up to a maximum temperature of 1200–1300 °C, making them not truly accident-tolerant. This could explain why the abbreviation "Advanced Technology Fuel" (ATF) is becoming more common [5].

Recently, the first attempts have been made to model the complex oxidation and degradation behavior of Cr-coated cladding, and the results are promising [21,25,26]. These models must be validated using experimental data. The effects of chromium thickness and the

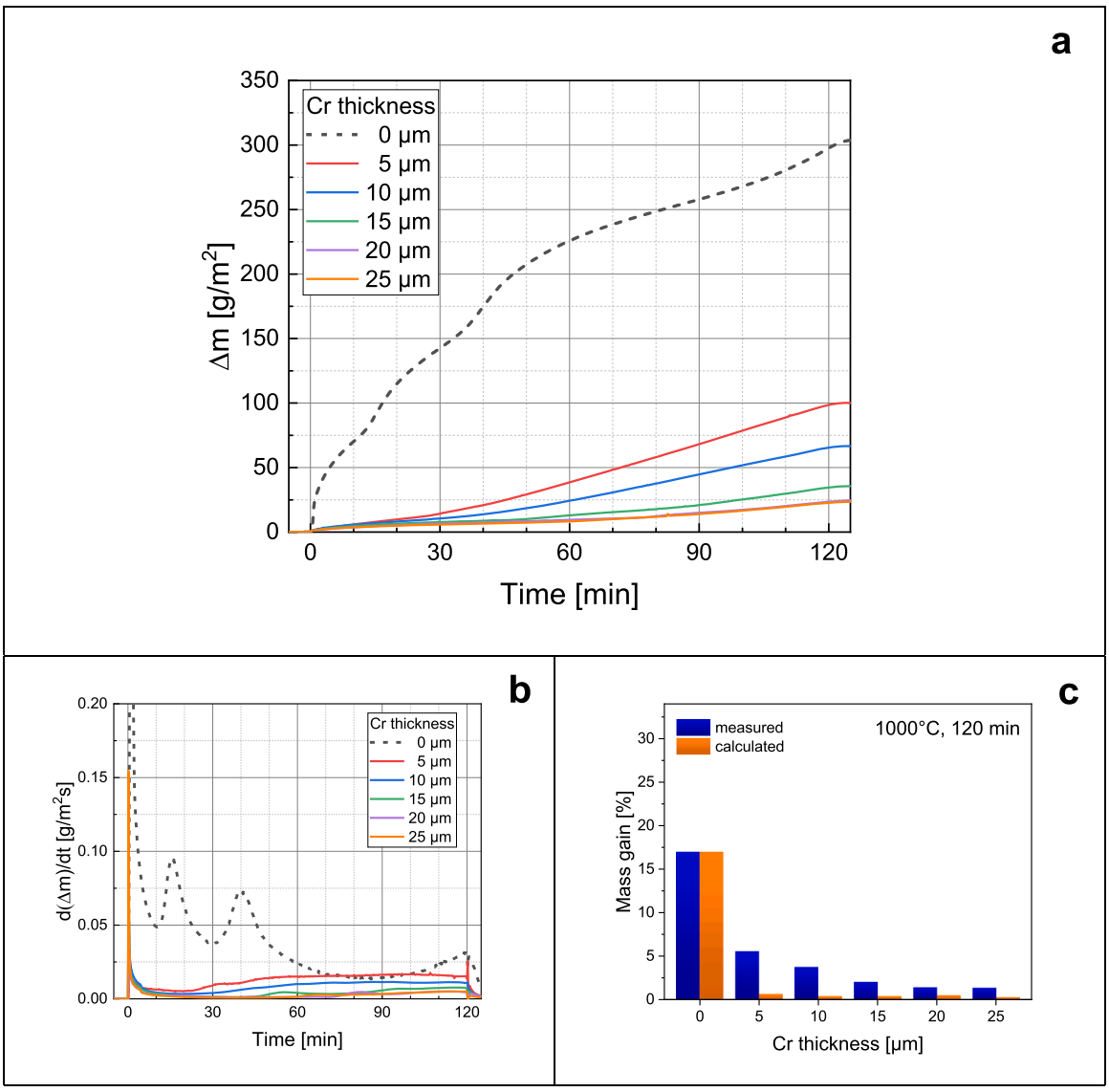

Fig. 4. Mass gain curves (TG (a), first derivative (dTG)(b), and final mass gain (c) after 2 hours at 1000 °C in steam. The mass gain diagram shows measured values (blue columns) and calculated values based on the post-test oxidation neglecting edge effects (see Appendix).

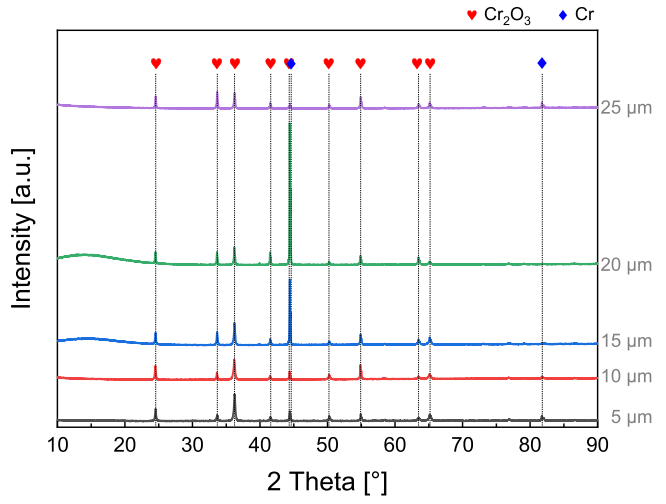

Fig. 5. X-ray diffractograms of the sample surface after 2-hours oxidation at 1000 °C.

microstructure of Cr coatings have been studied, for example, by Kashkarov [15], but only within a limited thickness range of 4.5 µm to 9 µm and up to 1200 °C. This paper presents a systematic study of the effect of Cr coating thickness within a more prototypical range of 5 µm to 25 µm on the high-temperature oxidation and degradation of Cr-coated Zircaloy-4 samples, both below and above the eutectic temperature at 1330 °C. This data can be used to validate models that take into account the oxidation and degradation of chromium-coated cladding tubes.

2. Experimental details

2.1. Samples

Zircaloy-4 (Zr-1.5Sn-0.2Fe-0.1Ni) plate specimens with the dimensions 10 × 15 × 0.65 mm^3 and a hole for sample suspension (diameter 2 mm) were used for all tests. The samples were polished and cleaned with acetone in an ultrasonic device. The Cr coatings were produced by magnetron sputtering using a Leybold Z 550 coater with a base pressure of 10^{-5} Pa. A 15-min plasma etching process was conducted using 500 W and 0.5 Pa argon in the deposition chamber. The subsequent stage involved the deposition of chromium coatings on both

Fig. 6. Cross section micrographs of the samples after 2-hours oxidation at 1000 °C.

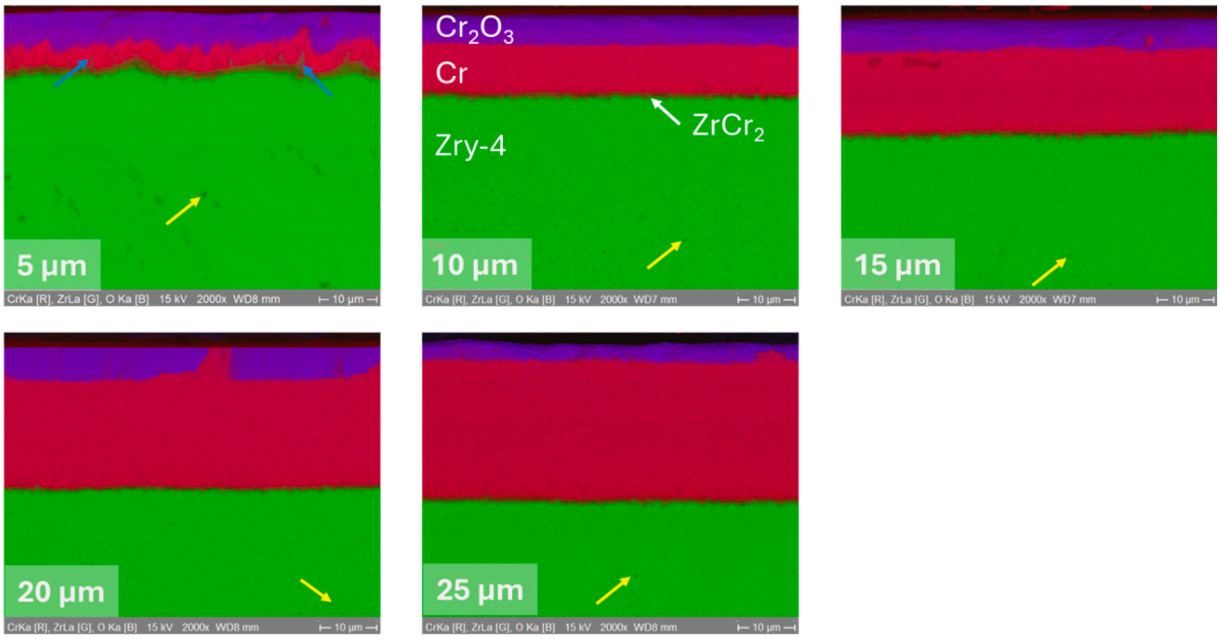

Fig. 7. EDS color mappings of the samples after 2-hours oxidation at 1000 °C. Yellow arrows indicate $ZrCr_2$ precipitates in the Zircaloy-4 bulk, blue arrows ZrO_2 paths along Cr grain boundaries.

main sides of the substrates. This process utilized a Cr target with direct current power set at 220 W and an atmosphere of 0.5 Pa Ar. Noteworthy is the absence of substrate rotation, bias, or heating during deposition. Each batch comprised 10 substrates. Different coating thicknesses (nominally 5, 10, 15, 20, and 25 µm) were achieved by adjusting the deposition time while maintaining a deposition rate of approximately 1.9 nm/s. The real Cr thickness of one sample of each group was measured using metallographic cross sections and taking 20–40 measurements per sample side with an optical microscope; the results are presented in Table 1. It can be seen that the targeted layer thickness of these specific samples was reasonably achieved at the investigated sample position for the 5-, 10-, and 25-µm samples, but was significantly higher for the 15-µm and 20-µm samples. This discrepancy likely arises from deposition rate fluctuations due to target erosion or plasma instability. Anyway, for the sake of simplicity, the samples are named according to their target chromium thickness in this paper.

2.2. *Experimental facilities and test conduct*

The experiments have been conducted in two different facilities: A

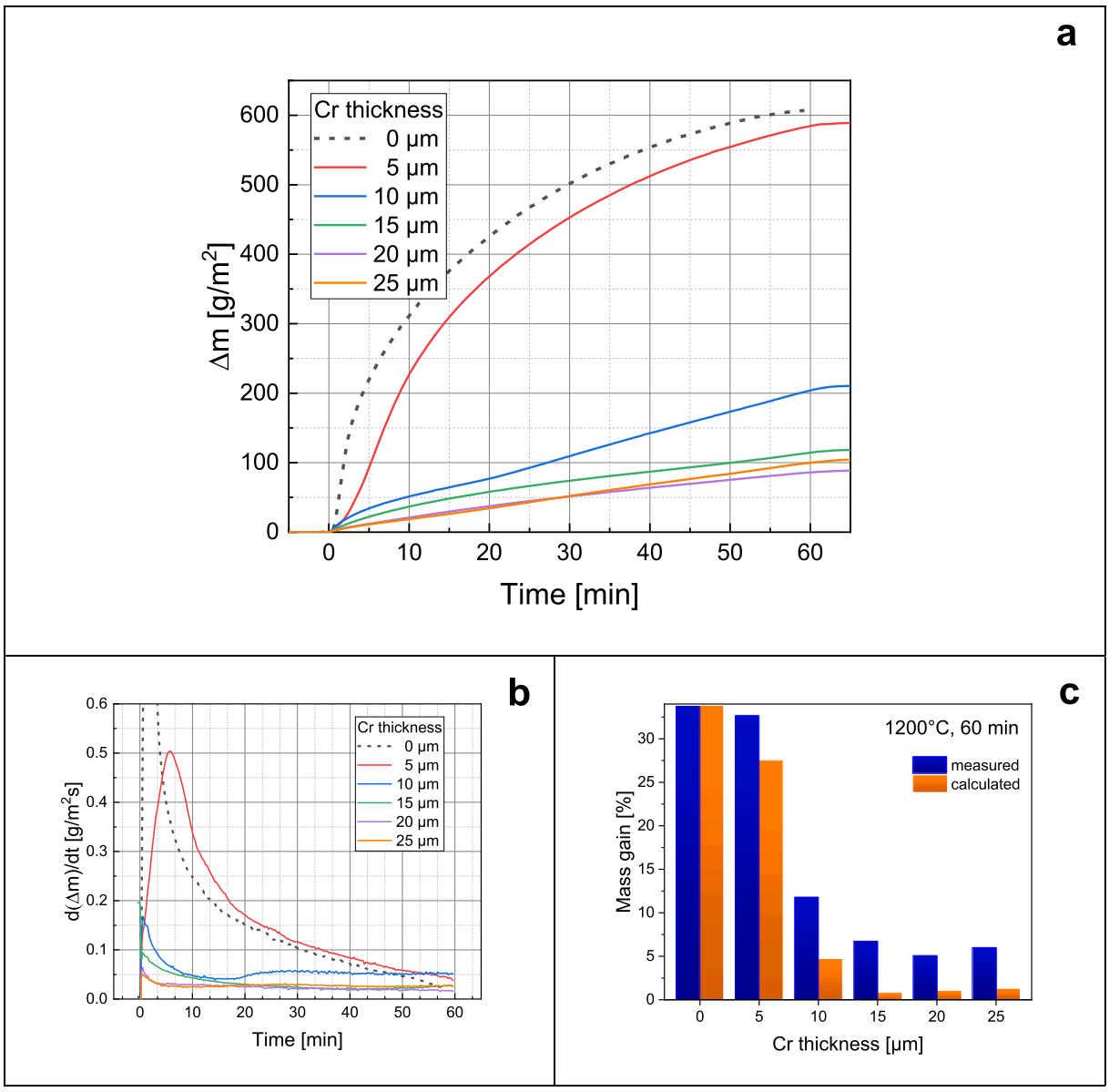

Fig. 8. Mass gain curves (TG)(a), first derivative (dTG)(b), and final mass gain (c) after 1 hour at 1200 °C in steam. The mass gain diagram shows measured values (blue columns) and calculated values based on the post-test oxidation neglecting edge effects (see Appendix 2).

commercial thermal balance (NETZSCH STA449 Jupiter F3) for experiments up to 1200 °C and an in-house developed horizontal tube furnace coupled with a mass spectrometer, Fig. 2. Detailed information on the test procedure is given in an earlier paper by the authors [27].

The STA449 is equipped with two furnaces, one "steam furnace" working up to 1250 °C in humid atmospheres including pure water steam and a "standard SiC furnace" working up to 1600 °C in dry atmospheres. The first was used in the thermo-gravimetric (TG) mode in these experiments connected to a steam supply system at the inlet and mass spectrometer (MS, Netzsch Aeolos Quadro) at the gas outlet. In these experiments, the MS is mainly used for process control, and the kinetic analyses are based on the mass change signal of the TG system. The test procedure included a heating phase to 1000 °C and 1200 °C, respectively, and a 10-min stabilization phase in pure argon (3 L/min, impurities <10 vppm), before steam (2 g/h) was switched on for the predefined isothermal oxidation phase, Table 2. The sample was only in contact with the steam flow, but not with the argon used as protective gas for the balance. Hence, the steam partial pressure was about 1 atm. The cooling occurred with nominally 100 K/min again in pure argon flow, but it was slower due to "natural" cooling of the furnace. An initial temperature overshoot was observed during the first three minutes after steam injection, especially for the non-coated sample at 1200 °C, due to the high enthalpy of oxidation and low steam flow rate. This temperature increase, probably by more than 100 K, resulted in a much higher initial oxidation rate, and therefore a higher final mass gain than would be expected in isothermal conditions. This effect was much less pronounced for the coated samples, which had lower oxidation rates, as well as for the experiments conducted in the BOX facility, which had much higher gas flow rates.

The BOX facility is a horizontal tube furnace (HTM Reetz GmbH, Berlin) with gas/steam supply and CEM (controlled evaporator and mixer) system (Bronkhorst High-Tech B.V.) and coupled to a sophisticated mass spectrometer GAM 3000 (InProcess Instruments Gesellschaft für Prozessanalytik mbH). The furnace can be equipped with a sample lock for the fast exchange of samples with the furnace being at temperature and defined gas flow, and hence very short heating and cooling times between room temperature and annealing temperature. For the oxidation experiments described in this paper, the furnace was heated to

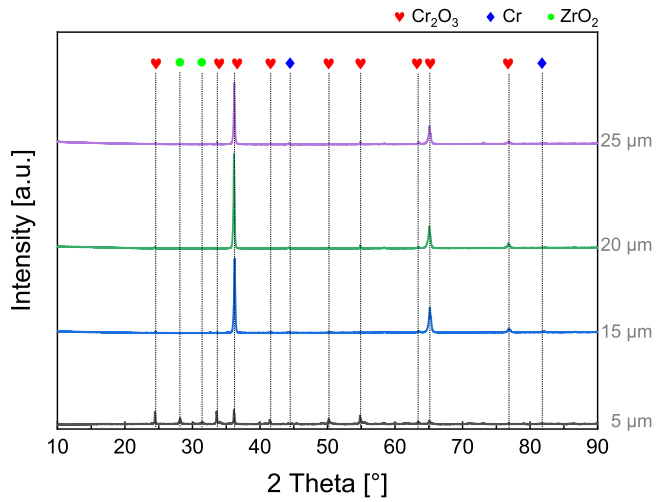

Fig. 9. X-ray diffractograms of the sample surface after 1-hour oxidation at 1200 °C.

500 °C for the transient phase, and to 1300/1400 °C for the isothermal tests in pure argon flow (20 L/h, impurities <10 vppm) before the samples were pushed into the hot zone. After 10-min stabilization in flowing argon, steam (20 g/h) was added until the end of the isothermal or transient oxidation phase. Steam was switched off and the sample was pulled into the sample lock where it cooled down to room temperature in a few minutes. The chosen argon and steam flow rates resulted in a H_2O partial pressure of about 0.55 atm. The mass spectrometer was calibrated for hydrogen using a certificated 95/5 Ar/H_2 mixture. Hence, using measured concentrations for hydrogen and argon as well as the known argon flow rate as reference, quantitative hydrogen release data were obtained and converted to in-situ mass gain data. Other gas species like H_2O, O_2, and N_2 were also measured for process control.

The duration of the isothermal tests was chosen to reach a reasonable oxidation including transition from protective to non-protective coating behavior but avoiding complete oxidation of the samples. Table 2 summarizes the test matrix with the main experimental parameters.

2.3. Post-test examinations

Samples masses have been determined before and after tests. Macrophotos were taken using a Canon EOS 1200D camera. Phase analyses of the sample surfaces were conducted using X-ray diffraction (XRD, Seifert PAD II). Then the samples were embedded in epoxy resin, ground and polished to proceed with metallographic analyses. The final step was done by OP-S polishing with 0.25 µm silica added acids for etching. The cross section for analyses is about 5 mm from the lower edge of the samples, i.e. should show typical coating behavior not affected by edge effects. The cross sections were examined by optical microscopy (OM, Leica DMC 4500) and Scanning Electron Microscopy (SEM), coupled with an Energy Dispersive X-ray Spectrometer (EDS, Philips XL 40S). EDS maps were taken for Zr, Cr, O, and Sn, but not for the minor alloying elements Fe and Ni. For the SEM analysis, the surface of the specimens was coated with a thin layer of carbon using a sputter coater (E5100, Bio-Rad Laboratories).

3. Results

3.1. Post-test appearance

Several sample features have been observed after the oxidation tests. The color is between gray and greenish, the latter originating from chromia. The light-gray surface of the uncoated sample after the test at 1000 °C is typical for breakaway oxidation. The uncoated 1200 °C sample was completely oxidized and broken after the test. The samples oxidized at temperatures beyond the eutectic temperature exhibit the typical “inverse crocodile skin” surface except the two samples with the thinnest Cr coating after the transient tests up to 1500 °C. This observation suggests that the metallic chromium was largely oxidized when temperatures reached 1330 °C. For the samples with crocodile skin, the ridges become larger and ridge network becomes less dense with increasing Cr thickness, which should be also connected to the increasing availability of metallic chromium for eutectic reaction.

In the following sections, the results are presented for each test condition, including mass change, TG and hydrogen release, XRD, optical microscopy (OM), and SEM/EDX. A large number of photos have been taken by optical microscopy and scanning electron microscopy,

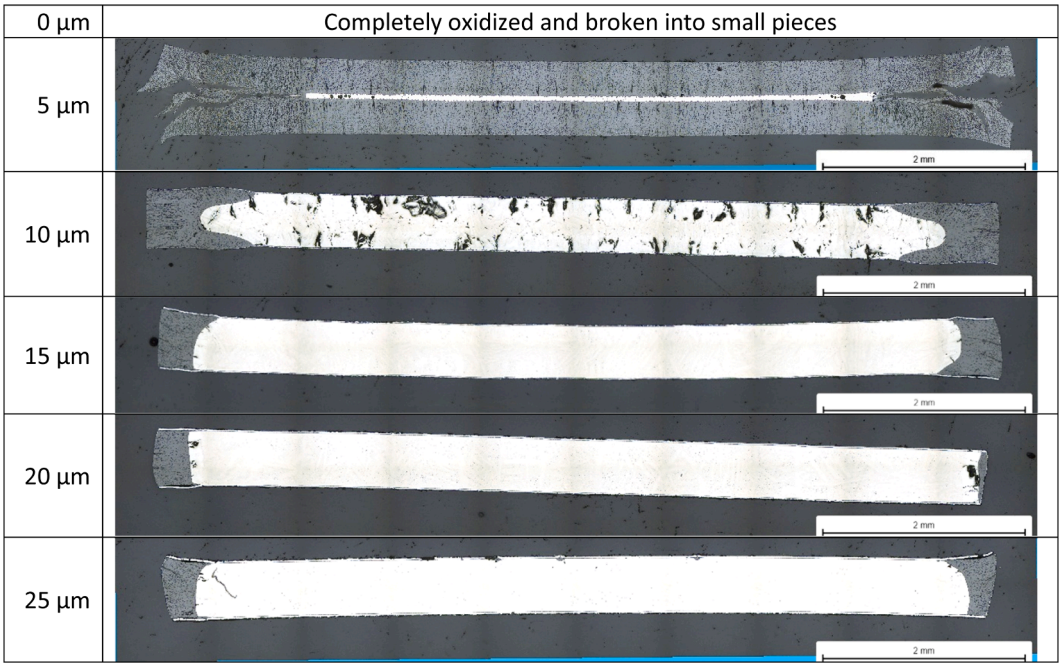

Fig. 10. Cross section micrographs of the samples after 1-hour oxidation at 1200 °C.

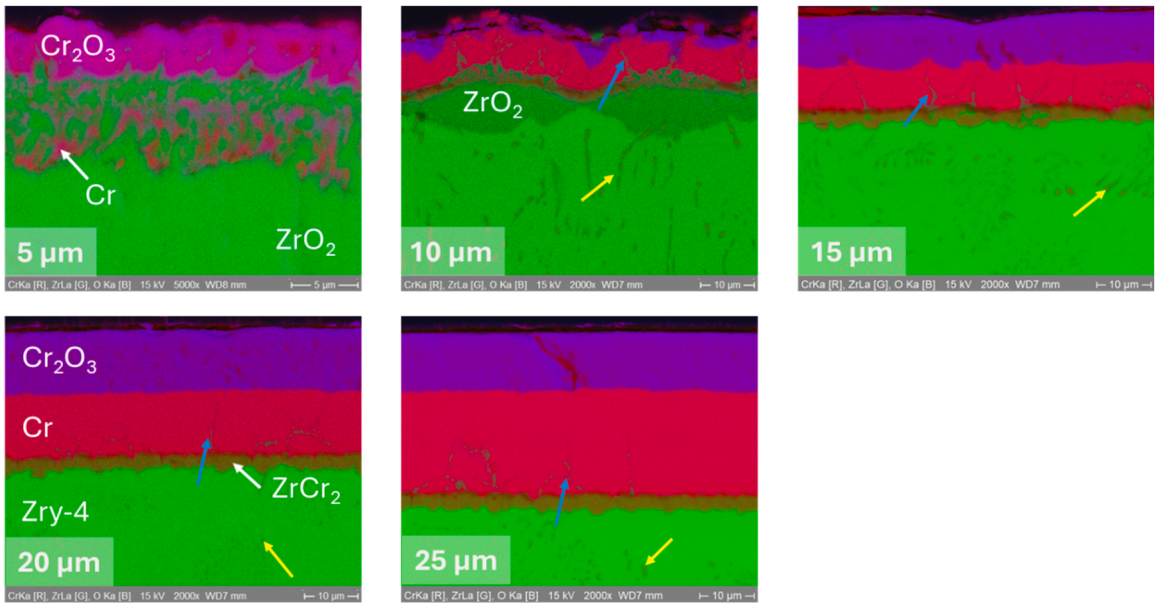

Fig. 11. EDS color mappings of the samples after 1-hour oxidation at 1200 °C. Yellow arrows indicate $ZrCr_2$ precipitates in the Zircaloy-4 bulk, blue arrows ZrO_2 paths along Cr grain boundaries.

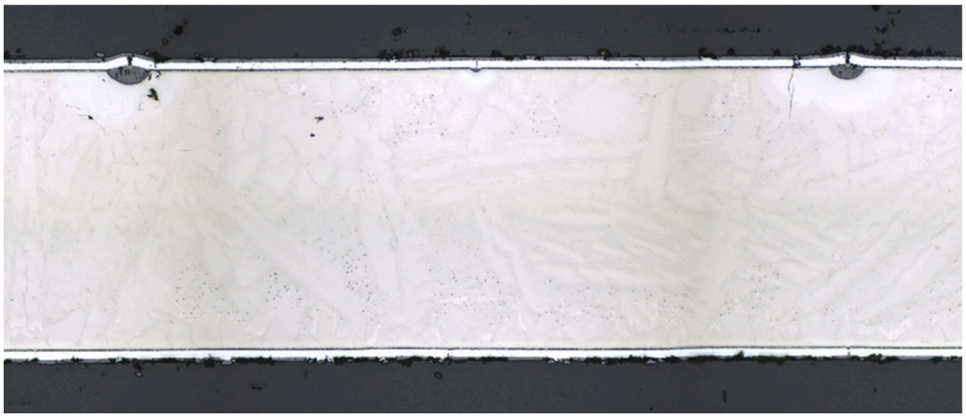

Fig. 12. Local failure positions of 25-µm sample after 1-hour oxidation at 1200 °C.

which cannot all be shown in the main part of this paper. A selection was made considering OM images of the whole sample cross sections, and SEM/EDS mappings focusing on the coating and bulk close to the coating for the samples tested at temperatures below the eutectic temperature and showing total cross section for the samples tested at 1400 °C and up to 1500 °C.

Appendix 1 shows more detailed analyses of selected cross sections with typical features.

3.2. *Isothermal tests at 1000 °C*

3.2.1. *TG results*

The TG curves as well as the integral mass gain values, Fig. 4, clearly show a protective effect of all Cr coatings. The mass gain due to oxidation of the coated samples is reduced to 33–8 % compared to the uncoated one with increasing initial Cr thickness. All TG curves of the coated samples are decreasing up to 20–25 min indicating fully protective coating. First deviation from this behavior with slowly increasing mass gain rates is observed after 22, 25, 45, 73, and 60 min for the samples with 5, 10, 15, 20, 25 µm coating thickness, respectively. All samples are only partly oxidized considering 35 wt. % mass gain for full oxidation of the bulk zirconium alloy.

The oscillating behavior of the mass gain rate of the non-coated sample is caused by breakaway oxidation. Protective zirconia is formed initially, and cracked due to the tetragonal-to-monoclinic phase change when a critical oxide thickness is reached allowing direct access of the oxidizing gas to the metal-oxide interface forming new protective oxide [28,29].

It should be mentioned here, and it will be discussed later in more detail (metallography and Appendix), that a stronger oxidation with the formation of ZrO_2 was found at the poorly coated edges of the samples, which, especially for the 1000 °C series, significantly contributed to the mass gain and have affected the transition times. So, the mass gains of the coated samples calculated based on the post-test oxidation status are only 2–4 % compared to the uncoated sample. However, the edge effects do not influence the general outcome of the experimental campaign, that's why the original online data are displayed and discussed in the main part of this paper. Fig. 4c provides measured mass gain values (blue columns) and calculated values based on the post-test oxidation neglecting edge effects.

3.2.2. *XRD results*

As expected, the X-ray diffractograms of the samples of the 1000 °C-series show mainly peaks of the superficial chromia layer and peaks of

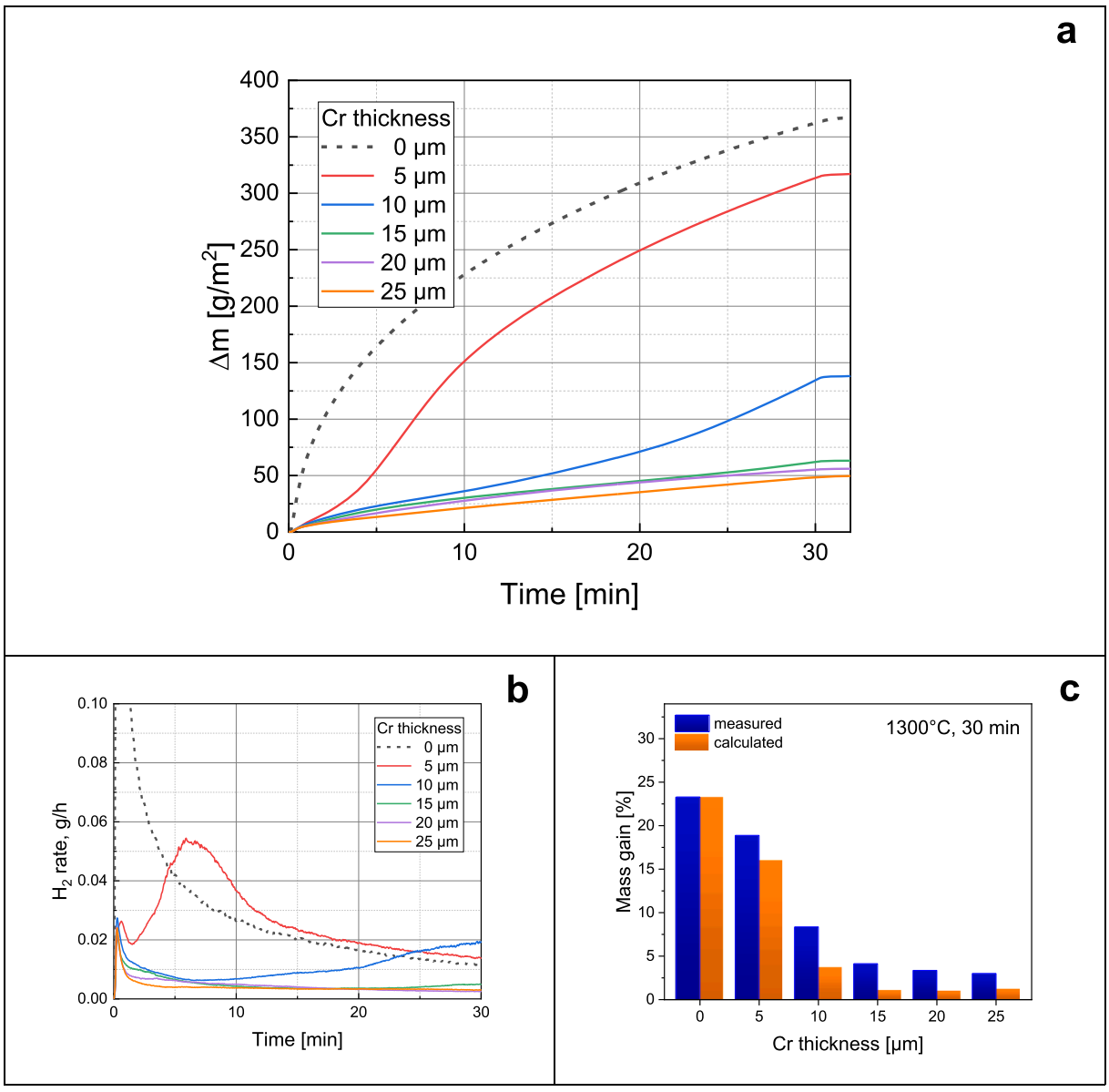

Fig. 13. Mass gain curves (converted from H_2 release data)(a), hydrogen release (corresponding to dTG)(b), and final mass gain (c) after 30 min at 1300 °C in steam. The mass gain diagram shows measured values (blue columns) and calculated values based on the post-test oxidation neglecting edge effects (see Appendix).

the underlying metallic Cr, see Fig. 5. Especially the samples with 15 and 20 µm Cr show a strong (202) texture of the chromia phase and significant intensity of the main peak of the metallic Cr phase.

3.2.3. *Cross sections*

The OM images of the total sample cross sections show the protective effect of all coatings from 5 to 25 µm Cr thickness compared to the uncoated sample, which is strongly oxidized for this temperature with typical porous breakaway oxide structure. The remaining metal of the coated samples is mainly prior β-phase converted to α-Zr with Widmannstätten pattern. Zirconium oxide was not formed on any of the coated samples, except at the edges where the chromium coating was poorer. These edge effects are analyzed and discussed in Appendix.

The EDS mappings with higher magnification focused on the coating confirm the typical four-layer structure with superficial chromia (Cr_2O_3), remaining Cr metal, a 1–2 µm thin $ZrCr_2$ intermetallic Laves phase and the Zircaloy-4 bulk. Tiny precipitates of $ZrCr_2$ are found in the Zry bulk. They are (most probably) formed during cooling below the solubility limit after diffusion of Cr into Zry at high temperature. The interfaces between the single layers are smooth for the samples with 10–25 µm coating thickness. The corresponding interfaces are wavy for the 5-µm sample with (almost) throughgoing ZrO_2 precipitates along the Cr grain boundaries as an indication for a starting transition from protective to non-protective behavior.

3.3. *Isothermal tests at 1200 °C*

3.3.1. *TG results*

A clear effect of the coating thickness on the oxidation is also observed at 1200 °C, Fig. 8. The mass gain of the 5-µm sample is almost the same as for the uncoated one. After only 2 min delay, the oxidation rate strongly increases and even exceeds the rate of the uncoated sample after 4 min until the end of the 1-hour oxidation time. The sample with 10 µm Cr coating exhibits a much lower mass gain compared to the 5-µm and uncoated samples, but a significantly higher mass gain than the samples with the thicker coatings. The oxidation rates of the 10-µm sample increase from approximately 18 min resulting in an about double final mass gain compared to the samples with 15–25 µm coatings. The

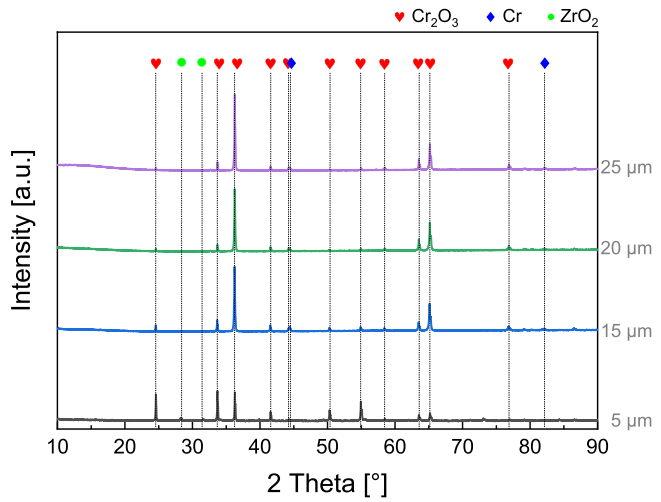

Fig. 14. X-ray diffractograms of the sample surface after 30-min oxidation at 1300 °C.

corrected values even show 4–6 times higher mass gain of the 10-µm sample, see Fig. 8c and Appendix 2. The samples with the coating thicknesses of 15, 20, and 25 µm show a very similar behavior with initially decreasing oxidation rates until 10–15 min and then more or less constant oxidation rates at low level until the end of the isothermal oxidation phase. The slightly higher mass gain of the 25-µm sample compared to the 20-µm sample could be caused by the edge effect and/or local coating failure as discussed in the next chapters. The calculated mass gains based on the post-test oxidation status (Appendix 2) show the same tendency, but an even more significant effect of the Cr thickness.

3.3.2. XRD results

The XRD diagrams, Fig. 9, show mainly Cr_2O_3 peaks with a significant (110) texture for the samples with 15–25 µm Cr coatings. Unfortunately, the measurement with the 10-µm sample failed. The intensity of the Cr_2O_3 peaks of the 5-µm sample is much lower with no pronounced texture. Furthermore, the most intense peaks of the monoclinic ZrO_2 phase are seen for the 5-µm sample, which is in correspondence with the high mass gain observed.

3.3.3. Cross sections

The cross-section overviews, Fig. 10, confirm the TG results, despite significant edge effects are also observed. The sample with initially 5 µm Cr coating is almost completely oxidized with an only about 50 µm thick remaining metallic core with precipitates of $ZrCr_2$. Higher magnifications and EDS mapping show, interestingly, here and on all strongly oxidized samples, a throughgoing, but porous chromia scale (about 3 µm thick on the 1200 °C samples) remained on the surface of the oxidized sample mainly consisting of zirconia, see Fig. 11. Below this chromia layer, a 5–7 µm thick mixed zone consisting of ZrO_2 and Cr_2O_3, follows. This could be the remnants of the fully oxidized $ZrCr_2$ intermetallic phase. Interestingly, despite the similar mass gain of the non-coated and 5 µm samples, and the fact that both were almost fully oxidized, the Cr-coated sample retained its geometry, whereas the non-coated sample broke into small pieces, as can be seen in Fig. 3. This could indicate a positive effect of chromium on integrity, even when fully oxidized.

A significant oxygen ingress into the Zry bulk took place through the degraded 10 µm Cr coating and resulted in the formation of more than 200 µm brittle oxygen-stabilized α-Zr(O) phase at both sides. A thin and non-homogenous layer of ZrO_2 is formed below the degraded coating. The remaining Cr-coating layer is interspersed with ZrO_2 paths, mostly throughgoing the layer thickness, and hence providing diffusion paths for oxygen. The samples with 15, 20, and 25 µm initial coating thickness show the four-layer structure with a 2–3 µm thick intermetallic $ZrCr_2$ phase. The ZrO_2 paths along the chromium grain boundaries are almost throughgoing for the 15-µm sample. Wavy interfaces indicate beginning transition from protective to non-protective coating. The layer interfaces of the 20-µm and the 25-µm samples are still smooth, and the ZrO_2 paths end right away from the Cr/Cr_2O_3 interface. Hence these coatings are still fully protective.

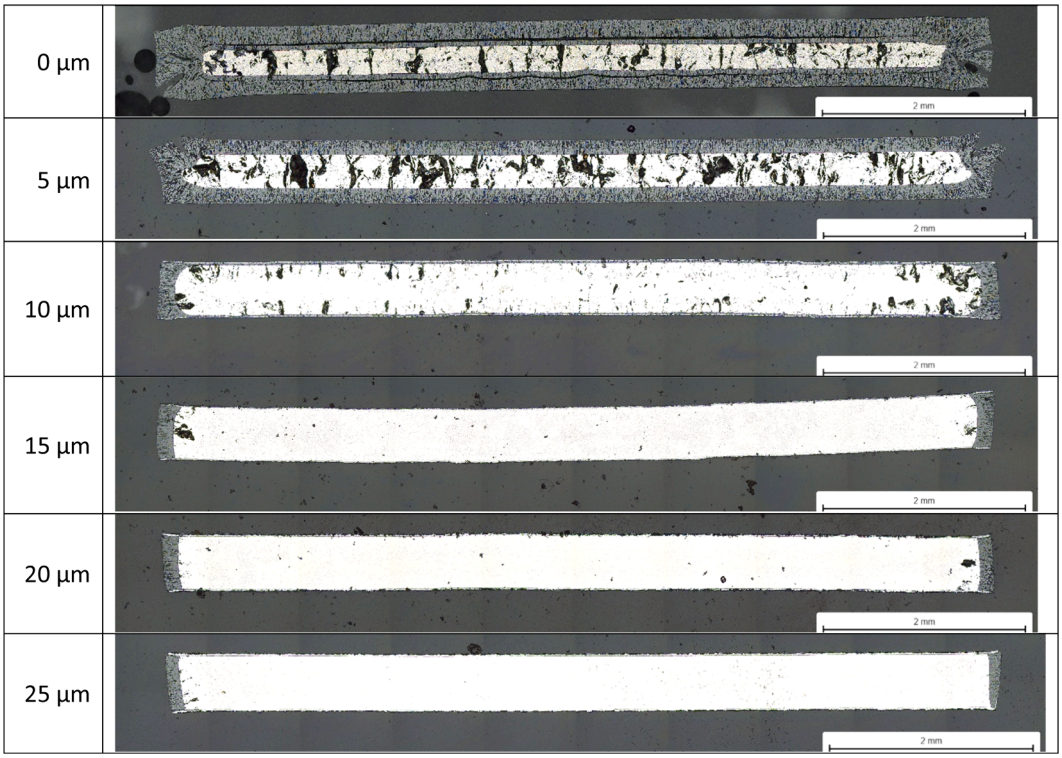

Fig. 15. Cross section micrographs of the samples after 30-min oxidation at 1300 °C.

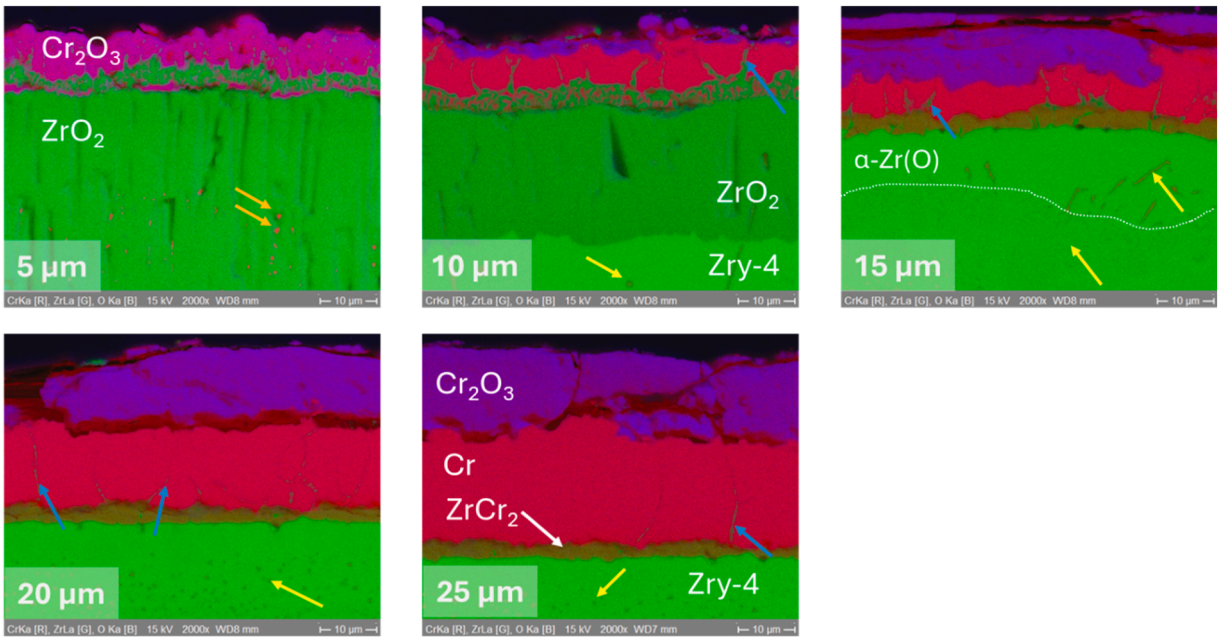

Fig. 16. EDS color mappings of the samples after 30-min oxidation at 1300 °C. Yellow arrows indicate $ZrCr_2$ precipitates in the Zircaloy-4 bulk, blue arrows ZrO_2 paths along Cr grain boundaries, and orange arrows Cr(-rich) precipitates in ZrO_2.

All Zry bulk metal contains $ZrCr_2$ precipitates. These are found along Zry grain boundaries and may be at least partially formed during oxidation and transition from β-Zr to α-Zr(O) with lower Cr solubility for the 10-µm sample. For the samples with protective Cr coating, the smaller point-like precipitates should have been formed during cool-down with decreasing solubility of Cr in Zry, see also Fig. A2 and Fig. A3 in Appendix 1.

Local failures of the Cr coating were observed for the 25-µm sample with semispherical ZrO_2 formation at the crack tips, see Fig. 12. These failures did not affect the adjacent coating and seem to have no serious effect on the sample oxidation as the TG curves confirm.

3.4. *Isothermal tests at 1300 °C*

The experiments at temperatures above 1200 °C were conducted in the BOX tube furnace connected to an accurate mass spectrometer. The hydrogen release data obtained by MS were converted to mass gain for better comparability with the TG tests as well as with literature data.

3.4.1. *Hydrogen release and mass gain*

At 1300 °C, just below the eutectic temperature, the effect of Cr thickness is also clearly observed as seen in Fig. 13. The 5-µm coating starts to fail after 1.5 min accompanied by a significant increase of mass gain. The mass gain rate becomes higher than for the uncoated sample after 4.5 min until the end of the isothermal oxidation phase, similar to the tests at 1200 °C. A slow increase in H_2 release rate starts after 7 min for the 10-µm sample and continues until the end of the oxidation indicating a steady degradation of the Cr coating. Towards the end of the test, the oxidation rate of this sample is higher than for the uncoated Zircaloy-4. A much smaller increase of the mass gain rate is observed for the 15-µm sample from about 22 min, whereas the samples with the thickest Cr coatings do not show any sign of transition from protective to non-protective behavior until the end of the 30-min oxidation at 1300 °C. The calculated mass gain values based on the post-test oxidation status without edge effects indicate a fully protective behavior even of the 15-µm sample, Fig. 13c.

3.4.2. *XRD results*

The X-ray diffractograms, Fig. 14, look very similar to the ones of the 1200 °C series. The main peaks can be assigned to chromia with a pronounced (110) texture for the samples with 15–25 µm Cr coatings and to a more equally distributed grain orientation for the 5-µm sample. Again, the 10-µm sample fell off the automatic sample changer during the measurement, and these data are missing. Minor peaks of Cr are seen for the 15–25 µm samples, and of ZrO_2 for the 5-µm sample.

3.4.3. *Cross sections*

The cross-section macrographs correspond well to the observed in-situ results of the oxidation tests and with the XRD results. The edge effects are comparably smaller.

Strong oxidation of the Zry-4 bulk took place for the uncoated sample and the sample with 5 µm Cr coating, Fig. 15. The remaining metal is mainly oxygen-stabilized α-Zr(O) as indicated by the large broken areas formed during the first grinding steps for metallographic preparation. In higher magnifications, tin enrichment (the "tin line") is seen in the middle of the thick ZrO_2 layers, Fig. A4. Cr-rich precipitates are found in the ZrO_2 layer between the tin line and the metal/oxide interface. Tin and Cr are also enriched in the very center of the remaining metal phase of the 5-µm sample. And, as already seen in the 1200 °C series, a porous and wavy, but throughgoing chromia layer is on the top of the thick zirconia layer, followed by a 3 µm thin two-phase layer consisting of ZrO_2 and Cr_2O_3, Fig. 16.

For the 10-µm sample, the layer order from the surface to the metal/oxide interface is 1) Cr_2O_3, 2) Cr interspersed with ZrO_2 paths along the grain boundaries, 3) ZrO_2/Cr two-phase mixture, and 4) a 30 µm thick ZrO_2 layer. These structures are the result of the already advanced degradation of the coating after 30 min at 1300 °C. The remaining metal part is roughly divided into three parts. α-Zr(O) is formed below the ZrO_2 from both sides dispersed with needle-like Cr-rich precipitates. Most probably $ZrCr_2$ has been formed during conversion of β-Zr into oxygen-stabilized α-Zr(O) at temperature. The inner third of the zirconium metal phase consists of a mixture of large prior β-Zr grains with and without fine Cr-rich precipitates, most probably formed during cooling, see Fig. A4 in Appendix 1. The Cr-rich parts also contain Sn.

The samples with 15–25 µm Cr coating show the four-layer structure typical for protective coating, even less clearly defined as at lower temperatures. The initial transition to non-protectiveness of the 15-µm coating seen in the hydrogen release curves becomes apparent in the

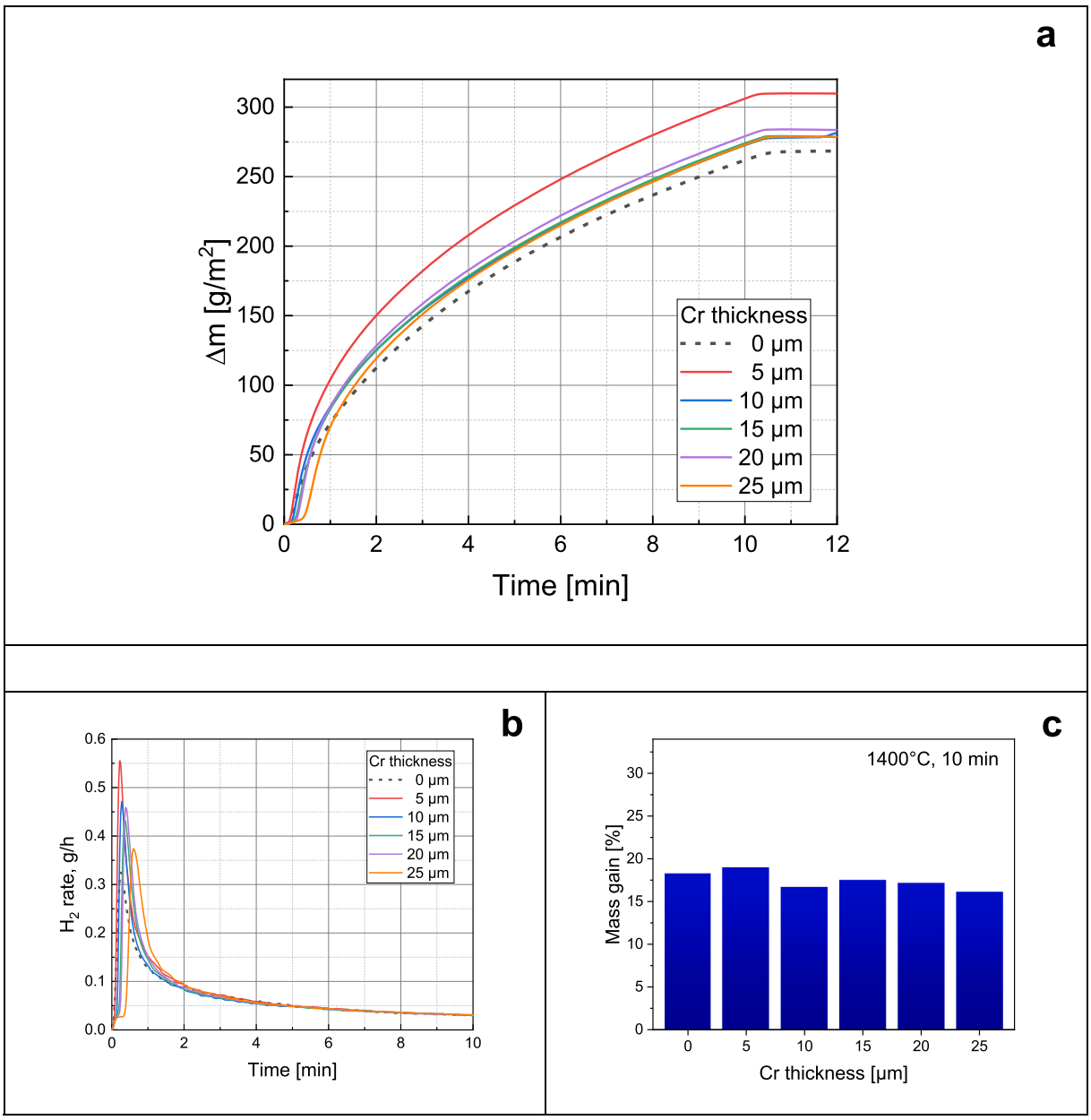

Fig. 17. Mass gain curves (converted from H_2 release data)(a), hydrogen release (corresponding to dTG)(b), and final mass gain (c) after 10 min at 1400 °C in steam.

formation of an around 10 µm thick α-Zr(O) layer with elongated Cr-rich precipitates, see dashed white line for the 15-µm image in Fig. 16. Smaller Cr-rich precipitates are seen in the β-Zr phase of the samples with initially thicker Cr coating. The ZrO_2 paths along the Cr grain boundaries go through relatively smaller parts of the Cr layer with increasing Cr thickness. The thickness of the intermetallic $ZrCr_2$ layer is 2–3 µm for the three samples with thicker coatings.

3.5. *Isothermal tests at 1400 °C*

3.5.1. *Hydrogen release and mass gain*

The hydrogen release and mass gain curves of the experiments at 1400 °C, i.e. above the eutectic temperature, look completely different compared to the ones obtained at temperatures below the eutectic, Fig. 17. All coated samples behave virtually like the non-coated one, which means that the coating lost its protective effect very initially. The oxidation kinetics is similar to the high-temperature oxidation of Zircaloy-4 determined by the growth of a semi-protective zirconia layer. The differences between the samples are only minor. So, a slight delay in accelerating oxidation is seen with increasing initial Cr thickness, maximal 20 s for the thickest coating. At the same time, the maximum hydrogen release (hence oxidation) rates are decreasing with increasing Cr thickness, however, they are all higher than for the non-coated Zry-4 sample. This may be related to increasing Zr-Cr eutectic melt formation taking time and consuming energy. However, the total mass gains of all samples are quite similar.

3.5.2. *XRD results*

The X-ray diffractograms of the samples of the 1400 °C series look very similar to each other with a mixture of Cr_2O_3 and ZrO_2, Fig. 18. The ZrO_2-peaks become slightly smaller with increasing Cr thickness indicating that a chromia layer is formed superficially becoming thicker with increasing initial Cr availability. The intensity ratios of the Cr_2O_3 peaks are close to the theoretical value, indicating an even distribution of grain orientation.

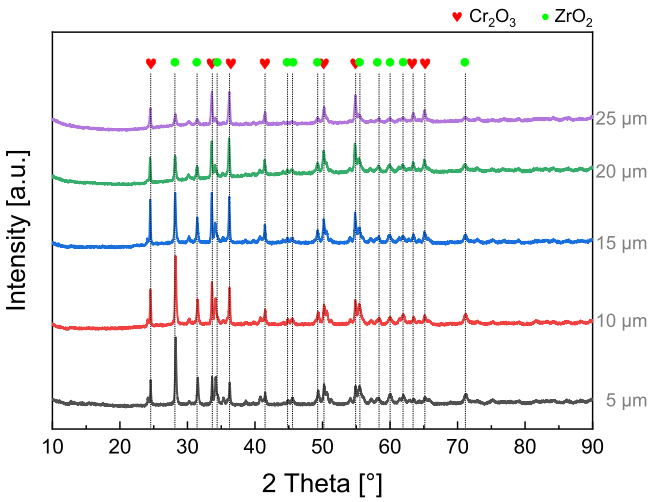

Fig. 18. X-ray diffractograms of the sample surface after 10-min oxidation at 1400 °C.

3.5.3. *Cross sections*

As expected from the in-situ and XRD results, the cross sections of the samples look similar with a 160–200 µm thick zirconia layer on all sample surfaces as seen in Fig. 19. The samples lost perfect rectangular shape with increasing Cr thickness due to the formation of eutectic melt. The EDS mappings with higher magnification in Fig. 20 show an increasing content in Cr-rich phases in the middle of the samples originating from frozen eutectic melt and, for the thicker Cr coatings, precipitated $ZrCr_2$. In the center of the samples with thicker Cr coating, Zry-4, most probably not molten, is surrounded by the frozen eutectic melt.

Higher magnification of the surface regions shows superficial chromia scales which become denser and thicker with increasing initial Cr thickness, and which look similar to Fig. 25 showing the surface of the 20-µm sample after the transient test. Tin enrichment is found approximately in the middle of the ZrO_2 layer (tin line), but with decreasing intensity with increasing initial Cr thickness. Furthermore, tin is enriched in the frozen eutectic melt in the Zr-rich phase, which is mixed with $ZrCr_2$ precipitates, Fig. A5.

3.6. ***Transient tests up to 1500 °C***

3.6.1. *Hydrogen release and mass gain*

In this test series, the eutectic temperature has been exceeded during heating with 10 K/min. All coatings exhibit initially a protective behavior resulting in significantly lower oxidation rates compared to the uncoated sample. First deviation to higher oxidation rate is observed for the 5-µm sample from 1080 °C which continuously accelerates and exceeds the oxidation rate of the uncoated sample at 1255 °C. Obviously, the thinnest Cr coating already transfers from protective to non-protective behavior before the eutectic temperature was reached due to the diffusion processes described in the introduction. A slight deviation from the other curves is also seen for the 10-µm sample at 1180 °C, though it is less significant. A fast transition to very high oxidation rates is observed for all samples with initial Cr thickness of 10 µm and more around the eutectic temperature between 1300 °C and 1340 °C rising with increasing Cr thickness. The oxidation rate of the uncoated reference sample is quickly surpassed by the coated ones, with maximum

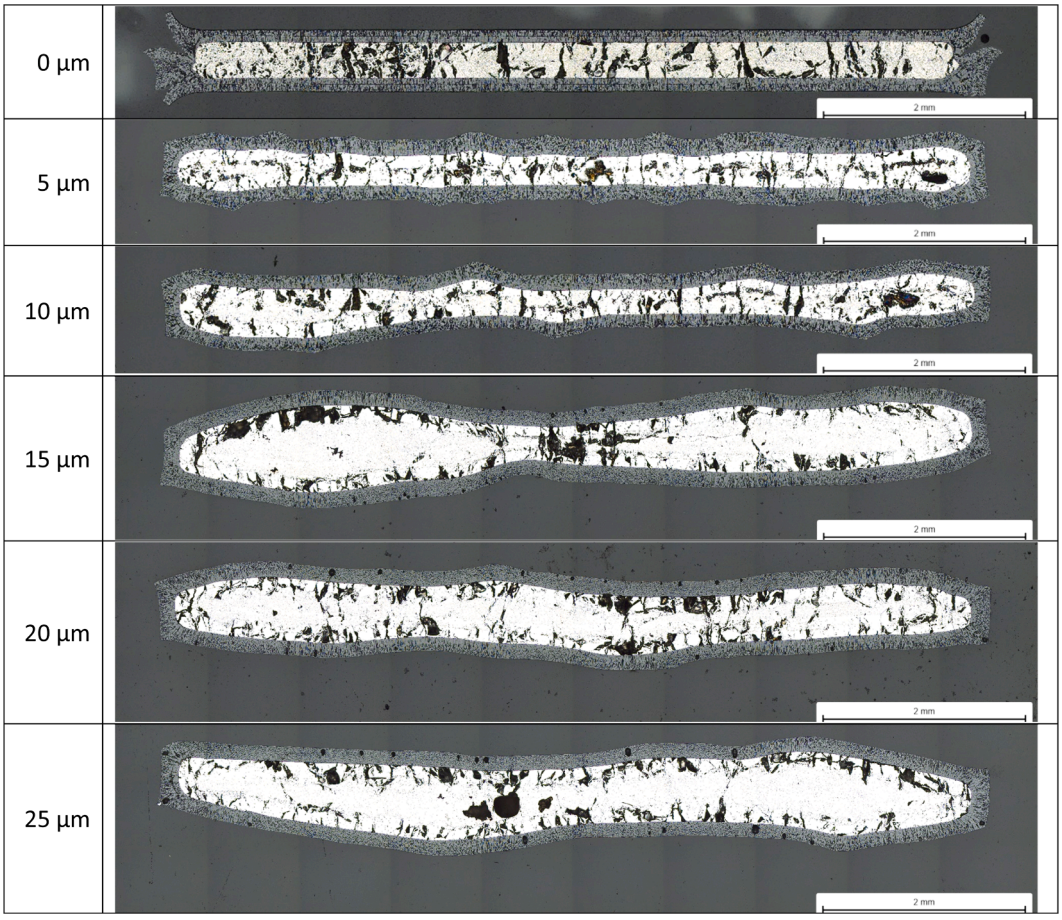

Fig. 19. Cross section micrographs of the samples after 10-min oxidation at 1400 °C.

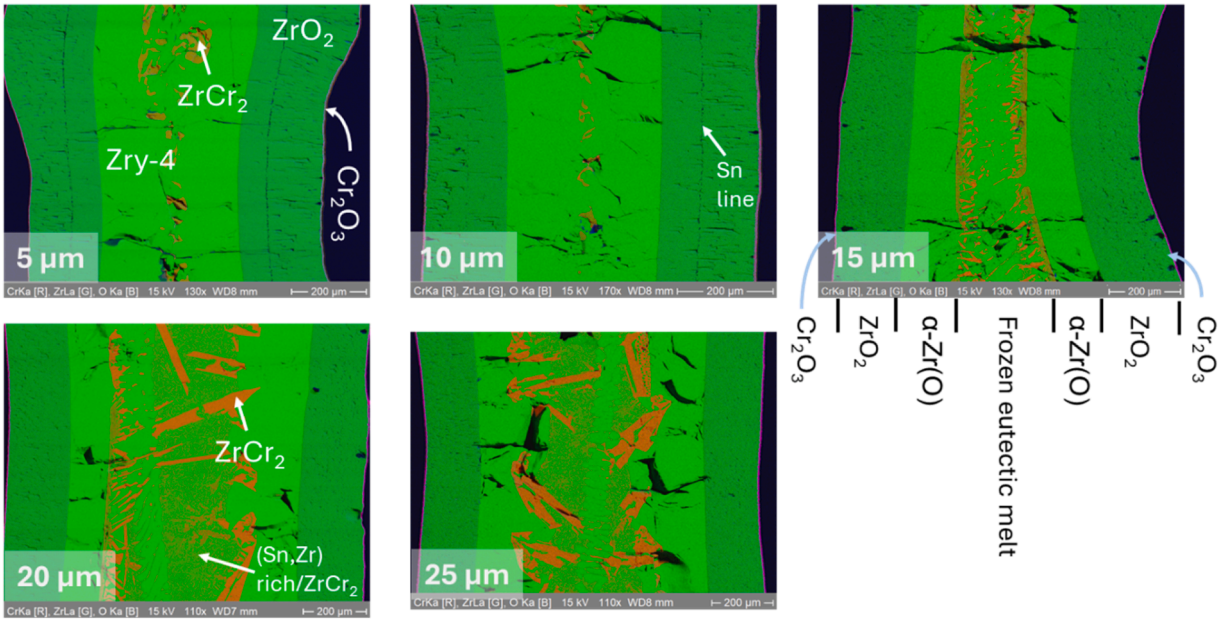

Fig. 20. EDS color mappings of the samples after 10-min oxidation at 1400 °C.

rates reaching three times higher than for the uncoated samples. The final mass gains of the samples are similar, with the ones for the uncoated and 5-µm sample being a bit higher than of the samples with thicker Cr coating (25 and 23 wt %, respectively) (Fig. 21).

3.6.2. XRD results

The X-ray diffractograms of all the samples taken after the transient tests are similar, showing mainly peaks of the non-textured Cr_2O_3 phase, Fig. 22. Only the 5 µm sample shows very small peaks of the monoclinic ZrO_2 phase.

3.6.3. Cross sections

The sample cross sections after the transient tests look similar to the 1400 °C series. Bending and deviation from the rectangular geometry are seen because of the strong oxidation and melt formation. The samples are strongly oxidized with an about 280 µm thick ZrO_2 layer for the uncoated and 5-µm samples, and 230–240 µm ones for the samples with thicker Cr coating, Fig. 23. An around 10–15 µm thick chromia layer is observed on top of the zirconia as expected from the XRD results and clearly visible on the overview EDS mappings in Fig. 24. Larger magnifications show that the "Cr_2O_3 layer" is rather a two-phase mixture of zirconia and chromia including an external layer of Cr_2O_3 with ZrO_2 precipitates, followed by ZrO_2 with Cr_2O_3 precipitates, and again a Cr_2O_3-enriched layer, see Fig. 25 as an example.

As for the samples of the 1400 °C-series, frozen eutectic melt is observed increasing with initial Cr coating thickness and hence availability of Cr. Tin is found in Zr-rich melt with $ZrCr_2$ precipitates but not in the Cr-rich melt. Furthermore, a pronounced tin line is seen in the zirconia layers, Fig. A6.

4. Discussion

The experiments presented in this study systematically investigated the effects of temperature and chromium thickness on the oxidation and degradation of Cr-coated Zircaloy-4 specimens. Both parameters have a strong influence on the behavior of the Cr coating under oxidizing conditions at high temperatures as seen in the graphical highlight image.

Due to the stronger oxidation of the poorly coated edges (edge effect), no in-situ kinetic data could be extracted from the mass change curves. However, the TG data, together with the comprehensive results of the post-test examination by various methods, provide a very clear picture of the coating behavior at high temperatures up to 1500 °C. A simplified summary of the results is given in Table 3, showing whether the coatings remained protective or failed under the tested conditions. The numbers provided for the tests below eutectic temperature are the calculated failure times according to Brachet's new ECrR criterion [21,30]. They are further discussed below.

The oxidation and degradation of the chromium coating is driven by various diffusion processes. Thus, the thicker the Cr coating, the longer it will provide protection at a given temperature below the eutectic point, and the higher the temperature, the shorter the protective effect of the coating. Above the eutectic point, all coatings failed almost immediately upon reaching the eutectic temperature, regardless of chromium layer thickness.

4.1. Scale structure and thickness

This general behavior is also reflected in the summary of the scale thickness diagrams shown in Fig. 26. As long as the coating is in the protective stage, the thickness of the formed Cr_2O_3 outer scale and of the $ZrCr_2$ intermetallic layer are approximately constant for the same experimental conditions. The formation of chromia is mainly controlled by the diffusion of Cr^{3+} cations through the growing oxide scale [31], and the formation of $ZrCr_2$ is controlled by the mutual diffusion of Zr and Cr and the limited mutual solubilities. Both processes should be independent of the initial Cr thickness as long as Cr consumption is not nearly complete, see also the later discussion of Brachet's ECrR criterion. Deviations from constant Cr_2O_3 and $ZrCr_2$ thicknesses and wavy interfaces are observed for samples where the coating is no longer (fully) protective. Here, Cr_2O_3/Zr redox reaction and oxidation of Zr and $ZrCr_2$ take place [14,18,32] and gradually cause a departure from the protective four-layer structure. The formation of oxygen-stabilized α-Zr(O) is the first indication of oxygen ingress through the coating. The coating is defined as "failed", if massive ZrO_2 formation is observed. The post-test appearance of our specimens at various stages of degradation is consistent with the results obtained by other groups and will not be discussed in detail in this paper.

The post-test appearance of the samples after testing beyond the eutectic temperature is completely different with thick ZrO_2 scales covered by thin Cr_2O_3 (-rich) scales. Both remain relatively consistent

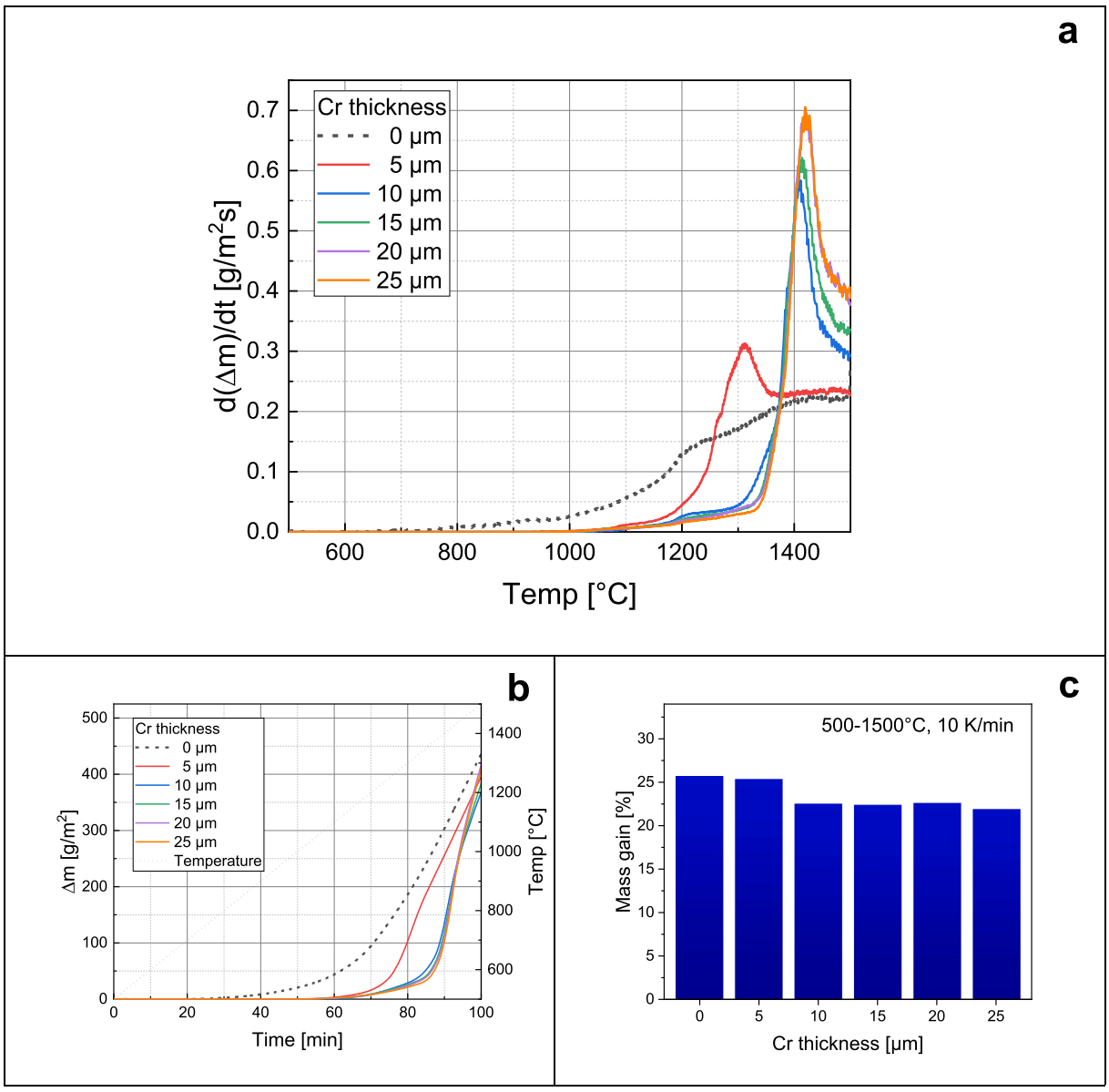

Fig. 21. Mass gain rate curves (converted from H_2 release data) versus temperature (a), mass gain versus time (b), and final mass gain versus initial Cr thickness (c) after transient tests from 500 to 1500 °C in steam.

within the experimental series. The superficial chromia layer is thicker after the transient tests because significant oxidation of the Cr coating occurred during the heating phase from 500 °C to 1330 °C before the eutectic reaction started. The heating phase was much shorter for the isothermal tests at 1400 °C during which the eutectic temperature was reached within seconds.

4.2. Degradation of the protective effect below eutectic temperature

The oxidation and degradation of Cr coatings below the eutectic temperature is primarily influenced by the diffusion processes. A well-adherent, highly protective chromia scale is formed during oxidation of the Cr coating. The rate-limiting mechanism is the diffusion of Cr^{3+} cations through the growing Cr_2O_3 scale [31]. Additionally, Cr diffuses into the Zr alloy matrix, which has relatively high solubility in the high-temperature β-Zr phase. The intermetallic $ZrCr_2$ Laves phase forms at the Zr/Cr interphase also by mutual diffusion. In parallel with these volume diffusion processes, Zr diffuses along the grain boundaries of the remaining Cr coating (with very low solubility of Zr) and is oxidized. This leads to oxygen diffusion paths through the metallic Cr layer to the Zry substrate. Additionally, redox reaction occurs between Zr and Cr_2O_3 (Equ.2) when the two components come into contact with each other, which leads to the counterintuitive effect of increasing Cr thickness and decreasing Cr_2O_3 thickness over time in the late transition phase. All these effects have been discussed in detail in literature, e.g. [14,18].

After the progression of scale thicknesses has been discussed in the previous subsection, this part analyzes the diffusion of Zr along Cr grain boundaries in relation to temperature and initial Cr thickness as they are visible in Fig. 7, Fig. 11, and Fig. 16 as well as in high-contrast EDS maps of zirconium in Fig. A1. Table 4 shows the quantitative data of ZrO_2 path length (absolute and relative) as well as the transition times, defined as times when the oxidation rates reached a minimum. These times are affected by the edge effects (Appendix 2) and just show a tendency.

For the samples tested at 1000 °C and 1200 °C, the path length absolute values are relatively constant meaning that the relative values are decreasing with increasing initial Cr thickness. Throughgoing ZrO_2 paths correspond to progressed transition from protective to non-protective coating behavior. At 1300 °C, close to the eutectic

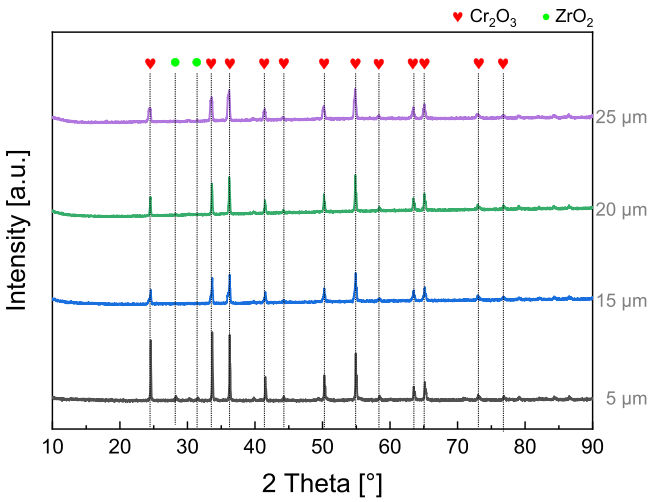

Fig. 22. X-ray diffractograms of the sample surface after transient tests from 500 to 1500 °C.

temperature, the diffusion processes are fast resulting in interfaces that are less well-defined and ZrO_2 paths deep into the remaining metallic Cr layer. However, the TG curves and the absence of ZrO_2 in the cross section mircrographs show a fully protective behavior of the coating until the end of the 30-min lasting oxidation for samples with initial coating thickness 15–25 µm.

The results presented in this paper correspond well with Brachet's ECrR criterion. This new metric (Equ.1) accounts for Cr coating consumption during high-temperature steam oxidation, through oxidation and diffusion of Cr into the underlying Zr alloy [21,30].

$$ECrR\ (\%) = 6.73{\cdot}10^{5}{\cdot}\exp\left(-\frac{15784}{T}\right){\cdot}t^{0.5}\Big/X_0 \quad (1)$$

The authors related this parameter to the LOCA embrittlement criteria, i.e., the post-quench strength and ductility of Cr-coated claddings and found a critical value of 70 % Cr consumption above which ductile-to-brittle transition (DBT) is observed. We applied this criterion to the experiments presented in this study, which focused on the chemical coating degradation and oxidation kinetics regimes. The numbers in the cells of Table 3 correspond to the times at which 70 % of the initial Cr coating has been consumed using the equation provided in [21]. These numbers show good agreement with the experimental results. For all coatings that have a protective effect until the end of oxidation, the calculated ECrR times are longer than the experimental ones and vice versa. A more detailed analysis of the data presented here, in the context of the ECrR criterion, is planned for publication in a separate paper [34].

4.3. Degradation of the protective effect above eutectic temperature

Beyond approximately 1330 °C, the degradation of the Cr-coated zirconium alloy is determined by (1) the almost instantaneous eutectic reaction between Cr and Zr resulting in the formation of melt, (2) the redox reaction of chromia with zirconium and Zr-containing melt,

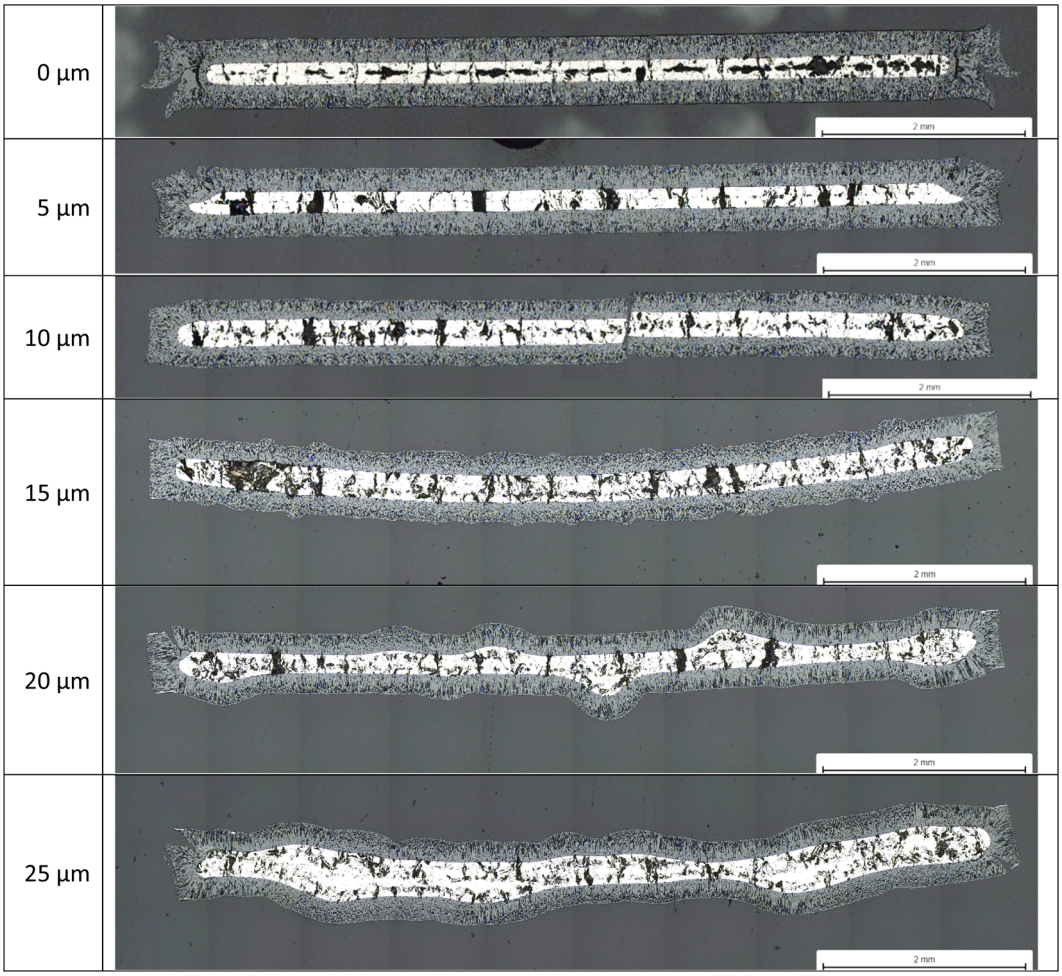

Fig. 23. Cross section micrographs of the samples after transient tests from 500 °C to 1500 °C.

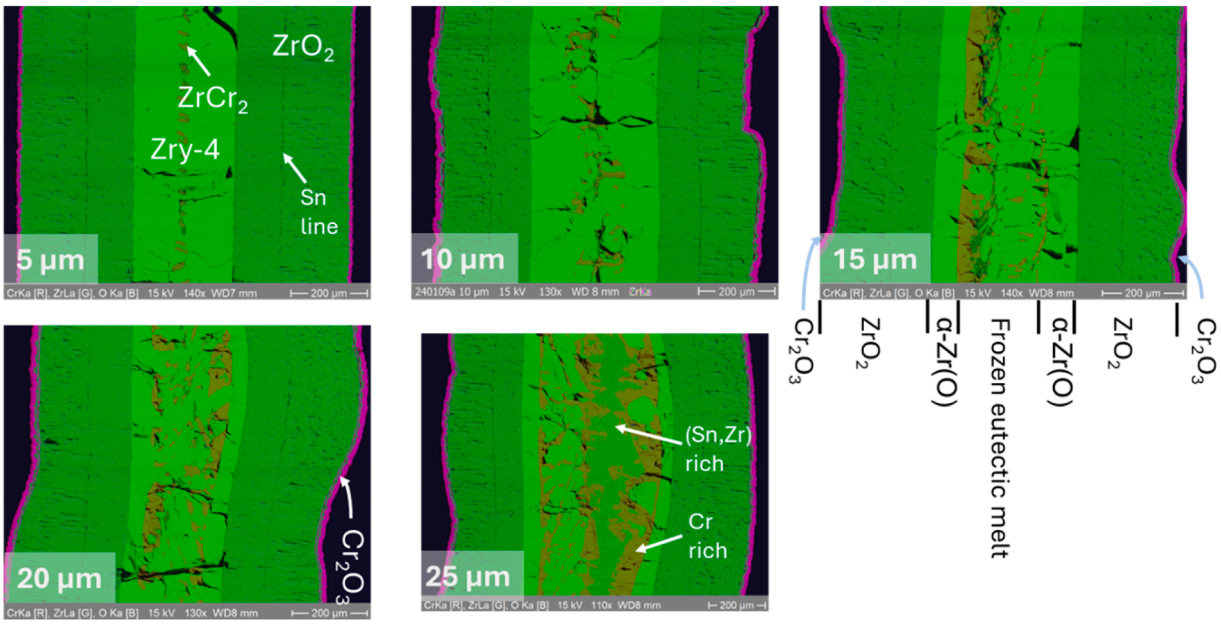

Fig. 24. EDS color mappings of the samples after transient oxidation from 500 °C to 1500 °C.

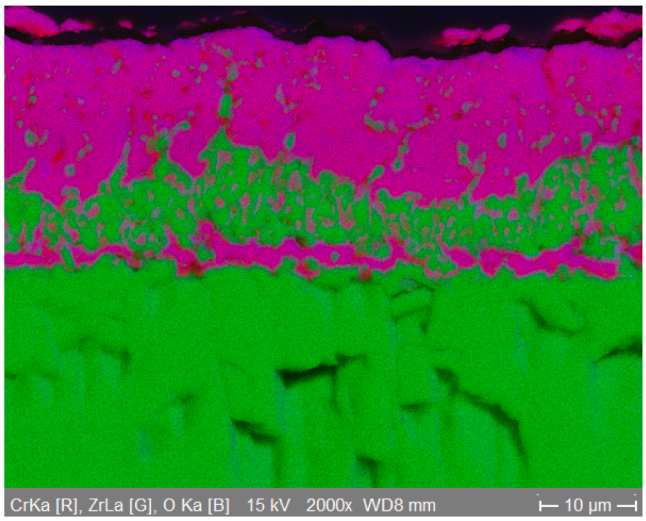

Fig. 25. EDS color mapping of the 20-µm sample after transient oxidation from 500 °C to 1500 °C. Magenta phase is Cr_2O_3, green phase is ZrO_2.

respectively, (Equ. 2) as well as (3) the oxidation of the non-protected Zry.

Samples that are heated beyond the eutectic temperature usually exhibit an inverted crocodile skin effect, i.e. the formation of ridges [14,16,19,35]. This was confirmed for all samples after isothermal testing at 1400 °C, as well as for samples with a thickness of 10 µm or more in the transient series up to 1500 °C. Throughout these tests, metallic chromium was available for the eutectic reaction with zirconium once the eutectic temperature had been reached. Based on Brachet's equation [21], the calculated Cr consumption during transient conditions (500–1500 °C at 10 K/min) is 7.4 µm at 1330 °C; therefore, no metallic Cr was available for the eutectic reaction for the 5-µm sample.

Various explanations of the origin of ridge formation can be found in the literature. Wang et al. [36] suggest a non-uniform eutectic reaction in the initial stage resulting in uneven mass distribution. Brachet et al. [14] refer to 'small displacement of the Zr-Cr eutectic film at the outer clad surface, induced by potential liquid "capillary" effects and local swelling associated with the solid-to-liquid volume change'. While there is no direct proof, post-test examinations in this study showed constant oxide thickness along the ridges and valleys of the sample surfaces. Based on these results, we believe that the crocodile skin formed very early on, when the eutectic temperature had been exceeded. The external chromia scale was reduced by the eutectic melt, with the resulting metallic Cr participating in the eutectic reaction. Due to the high surface tension of the Zr-Cr melt and its low viscosity [37], the melt contracts, forming ridges, and then oxidizes in this shape. This is a simplified picture; the real processes occur simultaneously and may be

Table 3
Summary of the protective behavior of the Cr coating as a function of temperature and Cr thickness. Dark green - protective, light green - beginning transition, orange - transition, red - not protective (failed). The numbers for the 1000, 1200 and 1300 °C tests represent the predicted failure times [min] according to Brachet's new ECrR criterion [21,30].

	5 µm	10 µm	15 µm	20 µm	25 µm
120 min, 1000°C	*265*	*1061*	*2387*	*4244*	*6631*
60 min, 1200°C	*9*	*37*	*82*	*146*	*229*
30 min, 1300°C	*2.3*	*9.4*	*21*	*38*	*58*
10 min, 1400°C					
500-1500°C					

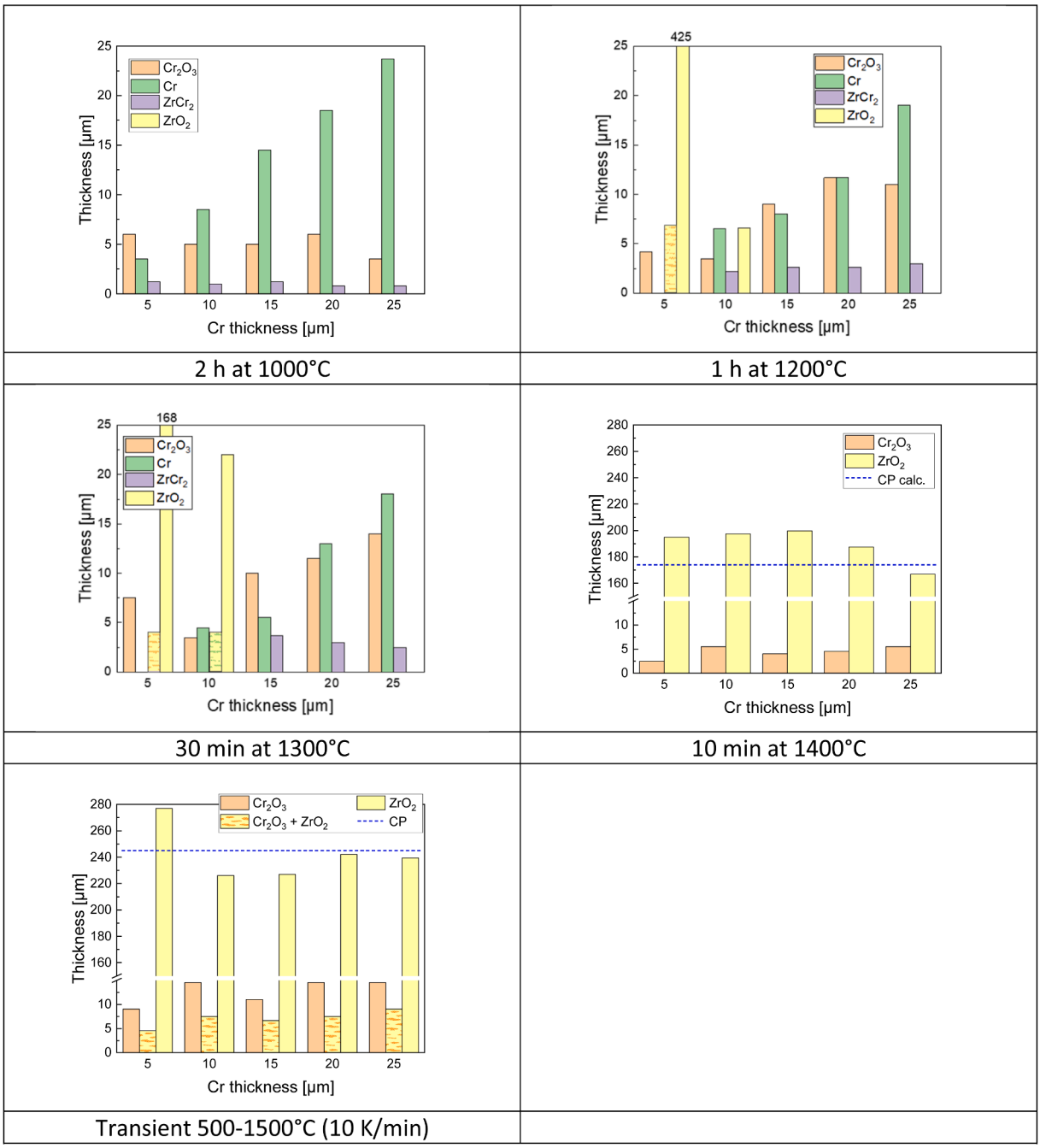

Fig. 26. Layer thicknesses of the tested samples. The dashed blue lines in the diagrams with $T>T_{eutectic}$ are the calculated ZrO_2 thicknesses with the Cathcart-Pawel correlation taken from [33].

more complex.

For the isothermal tests at 1400 °C, the oxidation kinetics between coated and non-coated samples is quite comparable because the initial conditions are quite similar after the rapid failure of the coatings. On the other hand, in the transient tests up to 1500 °C, the Zry oxidation starts with a non-protective, partly molten metallic surface after passing the eutectic temperature for the coated samples, whereas the uncoated sample at these conditions has already formed an approximately 140 µm thick ZrO_2 layer. Beyond 1330 °C, the oxidation rates of the (formerly) coated samples exceed those of the uncoated reference material. The accelerated kinetics are associated with an enhanced release of hydrogen and chemical energy, as reported in previous studies [16,23]. Consequently, the progression of corresponding accident scenarios may be significantly affected, also bearing in mind that the released chemical energy contributes to further heatup of the core.

As demonstrated in a recent paper by Kweon et al. [38], the thicknesses of chromium applied in this study are far below what is necessary to completely liquefy the cladding tube, so an immediate structural collapse should not occur. However, the cladding's mechanical stability is significantly reduced, so temperatures above the Zr-Cr eutectic point should be avoided. On the other hand, as has been observed and discussed in some previous papers [14,16,19], the frozen molten zone is embedded in a continuous, relatively uniform thick outer ZrO_2 layers. This feature is of practical interest since such outer thick and dense ZrO_2 layer may protect the molten zone from reacting with neighboring components in a representative bundle geometry.

A more or less throughgoing chromia layer on top of the thick zirconia layer is observed after both series above eutectic temperature.

Table 4
ZrO_2 path lengths (in μm and percentage of the metallic Cr layer thickness), and transition times from protective to non-protective coating behavior for the experiment below eutectic temperature.

Time& Temperature	Path length&Trans.	5 μm	10 μm	15 μm	20 μm	25 μm
2 h, 1000 °C	**ZrO_2 path**	2.5–3.0 μm				
		80–100 %	30 %	20 %	15 %	12 %
	Transition*	20 min	22 min	42 min	71 min	40 min**
1 h, 1200 °C	**ZrO_2 path**	-	7.0–7.5 μm			9–10 μm
		-	100 %	90–100 %	60–65 %	50 %
	Transition*	< 1 min	18 min	40 min	nt	15 min**
0.5 h, 1300 °C	**ZrO_2 path**	-	5 μm	5 μm	10 μm	15 μm
		-	80–100 %	80–100 %	80–100 %	80 %
	Transition*	1.5 min	6.5 min	18 min	nt	nt

* Affected by edge effects
** Very slow transition
nt = no transition

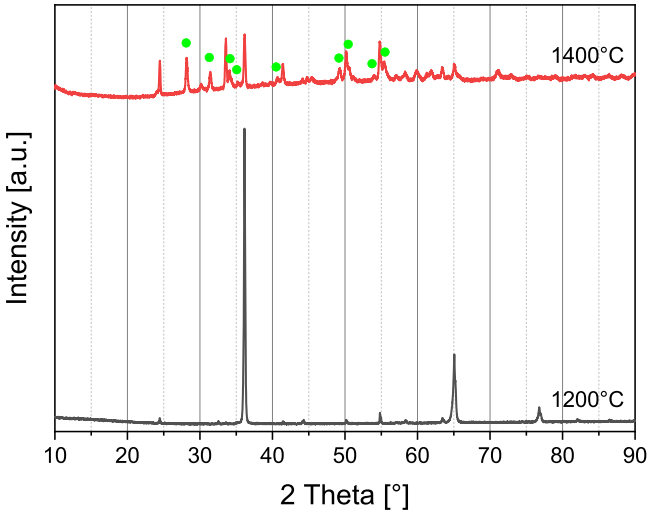

Fig. 27. XRD diagrams of the 20-μm samples after oxidation at 1200 °C and 1400 °C. The green points indicate ZrO_2 peaks, all other belong to Cr_2O_3.

These chromia layers should not be the initially formed ones as indicated by the XRD results. The chromia scales formed during isothermal tests below eutectic temperature are strongly textured. This Cr_2O_3 texture results from solid-state epitaxial oxidation. At the latest, when the eutectic temperature is reached and the chromia is in direct contact with the eutectic Zr-Cr melt, the initially formed Cr_2O_3 is reduced by Zr, which has a much higher affinity for oxygen, see Equ. 2.

$$2Cr_2O_3 + 3Zr \rightarrow 4Cr + 3ZrO_2 \quad (2)$$

The superficial metallic Cr produced by the redox reaction between Zr and Cr_2O_3 is thermodynamically unstable in oxidizing environment at high temperatures and does not persist. When disconnected from the metallic zirconium, it re-oxidizes to Cr_2O_3, Equ.3. Since the interface is now disrupted and contains ZrO_2, the oxide does not regrow epitaxially. The resulting Cr_2O_3 is fine-grained, porous, and intermixed with ZrO_2, and it is no longer protective. The comparison of the X-ray diffractograms for 20-μm coated samples clearly shows strongly textured chromia below eutectic temperature and chromia with random grain orientation after eutectic interaction at 1400 °C as well as the intermixed ZrO_2 (Fig. 27).

$$2Cr + 3H_2O \rightarrow Cr_2O_3 + 3H_2 \quad (3)$$

The ZrO_2 thicknesses after the experiments above the eutectic temperature reasonably agree with the calculated values with the Cathcart-Pawel correlation for 10 min at 1400 °C and transient with 10 K/min from 1330 °C to 1500 °C as indicated by the dashed lines in Fig. 26. The slightly higher measured oxide thickness for the samples with 5–20 μm Cr after the isothermal tests at 1400 °C could be due to the more intensive initial overshooting of the reaction rates for these samples compared to the non-coated sample, Fig. 17. Higher oxidation rates correspond with higher chemical energy release, which resulted temporarily in a temperature increase.

According to the Zr-O phase diagram [39], an oxygen-stabilized α-Zr(O) phase is observed below the ZrO_2 layer as in the uncoated Zr alloy. The solubility of Cr in α-Zr is very low; therefore, chromium is pushed into the remaining β-Zr phase. Depending on temperature and composition, it forms a eutectic melt there, and $ZrCr_2$ precipitates latest during cooling. As the initial Cr coating thickness increases, the content of previously molten Cr-rich phases increases, as seen in Fig. 19, Fig. 20, Fig. 23, and Fig. 24.

4.4. Consequences for reactor safety

This study confirms that a Cr coating can significantly improve the oxidation resistance of Zr-based alloys at temperatures of up to 1300 °C for a certain period of time. Degradation is strongly dependent on temperature and is mainly determined by diffusion-driven mechanisms such as oxidation and mutual solubility, which lead to a slow transition from protective to non-protective behavior. Consequently, the thickness of the Cr coating is an important factor in determining how long it remains protective. The thicker the coating, the greater the protective effect. However, the results of this study also showed that very high coating thicknesses can lead to a thermomechanical mismatch between the coating and the underlying material. This mismatch can result in cracks forming in the coating, through which localized oxidation attacks can occur. The optimum thickness for a PVD Cr coating, as tested in this study, appears to be 15–20 μm.

The Cr coating loses its protective effect completely and almost instantaneously above the eutectic temperature in the Zr-Cr system. The oxidation kinetics change from chromia formation to zirconia formation. This can easily be incorporated into models of the oxidation and degradation of Cr-coated ATF cladding in accident scenarios. The data obtained in this study can be used to validate the development of the corresponding model. A separate paper is planned on the validation of Brachet's new ECrR criterion with the experimental data of this study [34]. First results of this analysis have been recently published at the 30th International QUENCH Workshop [40]. In general, Cr coatings can significantly improve performance during operation, operational transients and DBA LOCA scenarios. However, in BDBA scenarios, Cr-coated cladding is not accident tolerant at all because it loses its protective effect beyond approximately 1330 °C.

5. Conclusion

This study systematically evaluated the effect of chromium coating

thickness (5–25 μm) on the high-temperature oxidation and degradation of Cr-coated Zircaloy-4 up to 1500 °C, i.e. below and above the eutectic temperature in the system Zr-Cr. The experiments confirm the strong influence of both temperature and coating thickness on the protective behavior of the coatings, providing valuable data for model development and validation. The key outcomes are:

- Below the eutectic, Cr coatings significantly delay oxidation compared to uncoated Zircaloy-4. The level of protection increases with coating thickness, with the optimum range for PVD coatings identified as 15–20 μm. Coating degradation is governed by diffusion-controlled processes, including oxidation, mutual solubility, and Zr grain boundary diffusion. These gradually lead to the loss of protectiveness, with transition times strongly dependent on coating thickness and temperature.
- Once the eutectic temperature is exceeded, all coatings lose their protective function almost instantaneously, independent of thickness. Oxidation kinetics then switch from chromia to zirconia formation, accompanied by accelerated hydrogen release and chemical heat generation. The inverse crocodile skin surface is formed very initially due to the high surface tension of the formed eutectic melt. The remaining chromia layer found on the top of the zirconia scale is re-formed after consumption of the initially formed Cr_2O_3 by the Zr/Cr_2O_3 redox reaction and later re-oxidation of the metallic Cr close to the surface.
- Cr coatings can markedly improve cladding performance during normal operation, transients, and design-basis accident (DBA) conditions. However, in beyond-design-basis accidents (BDBA) exceeding the eutectic point, they cannot be considered accident tolerant.

In summary, Cr coatings represent an effective near-term ATF solution with substantial benefits up to ~1300 °C. Their intrinsic limitation at higher temperatures must, however, be explicitly considered in accident analyses and safety assessments.

CRediT authorship contribution statement

Martin Steinbrueck: Writing – original draft, Visualization, Validation, Supervision, Project administration, Methodology, Formal analysis, Data curation, Conceptualization. **Injae Lee:** Validation, Investigation, Data curation. **Ulrike Stegmaier:** Writing – review & editing, Investigation. **Chongchong Tang:** Writing – review & editing, Validation, Investigation, Data curation. **Michael Stueber:** Writing – review & editing, Resources.

Declaration of competing interest

The authors declare that they have no known competing financial interests or personal relationships that could have appeared to influence the work reported in this paper.

Acknowledgement

One author received funding from the Korea Nuclear International Cooperation Foundation (KONICOF) for a six-month internship at the Karlsruhe Institute of Technology (KIT).

Appendix 1. More detailed metallographic images of selected samples

ZrO2 paths in the Cr layer

The EDS Zr maps with high contrast in Fig. A1 illustrate the ZrO_2 paths along the grain boundaries in the Cr scales for samples after tests. For each temperature below the eutectic temperature, three images with Cr thicknesses around the transition from protective to non-protective behavior of the coating were selected.

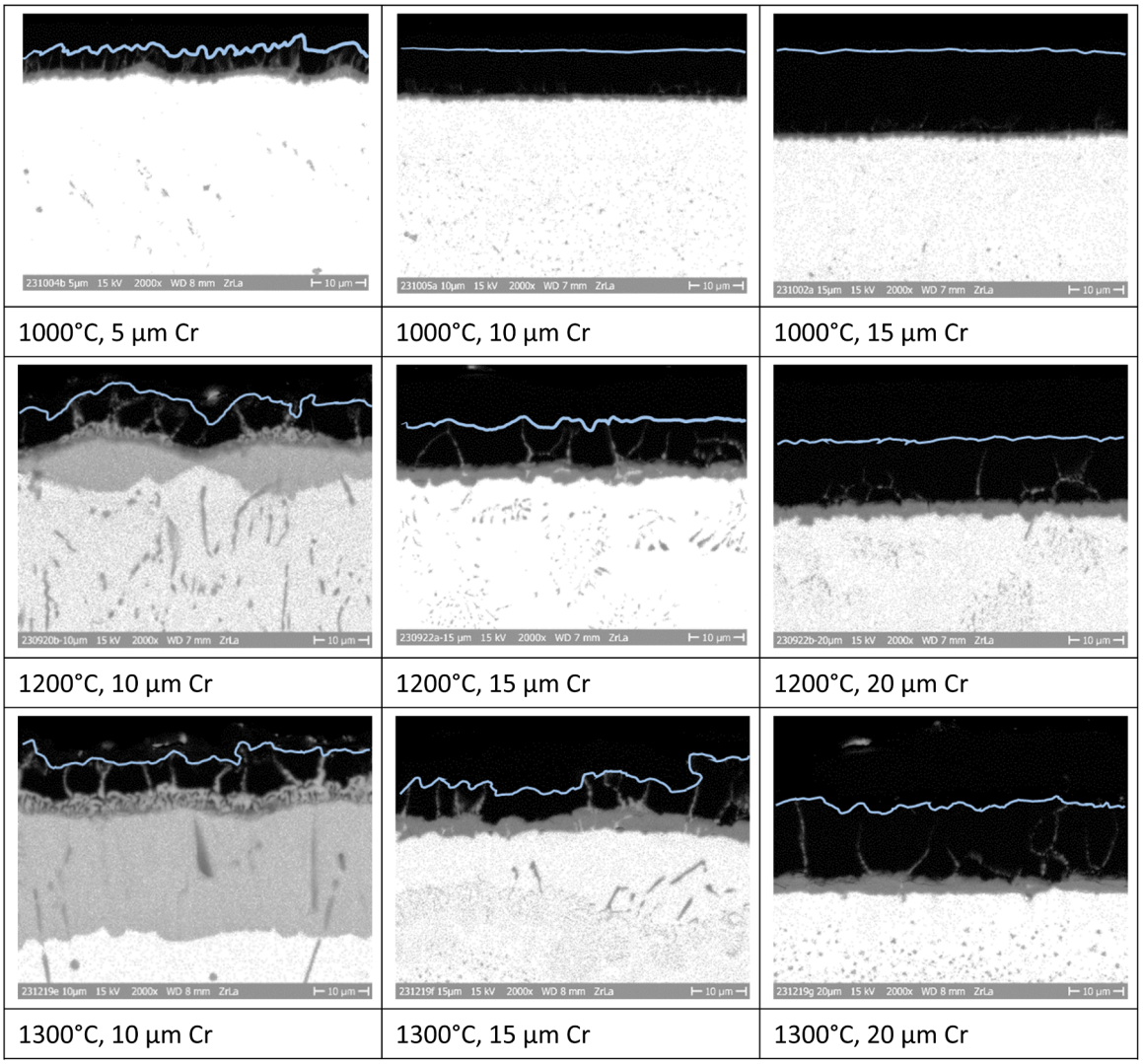

Fig. A1. High-contrast EDS Zr maps showing the ZrO_2 paths in the Cr scales. The light-blue lines indicate the interface Cr/Cr_2O_3.

Metallographic details of the 20-µm sample after the oxidation test at 1200 °C

The optical micrograph with a high magnification of the coating area in Fig. A2 and the EDS Cr map of the whole sample cross section in Fig. A3 provide additional information on the 20-µm sample after the test at 1200 °C. The OM image confirms the 4-layer structure. The ZrO_2 paths along the grain boundaries of the metallic Cr coating are clearly visible. The grains of the $ZrCr_2$ layer are partially broken out due to the high hardness of such intermetallic Laves phases. Both images show the formation of $ZrCr_2$ precipitates in the substrate. The precipitates exhibit a characteristic 4-fold symmetric morphology, indicative of crystallographically directed growth along preferred ⟨100⟩ or ⟨111⟩ directions during cooling, as Cr solubility in α-Zr decreases and supersaturation leads to diffusion-controlled precipitation of the cubic C15 Laves phase. These $ZrCr_2$ precipitates are not seen close to the coating/bulk interface, probably due to a slightly higher oxygen content there promoting α-Zr(O) formation reducing Cr solubility and/or mobility. The $ZrCr_2$ precipitates are distributed throughout the bulk with a slight gradient towards the Zry-4 plate. This is consistent with the high solubility of Cr in β-Zr and solid-state precipitation upon cooling. In addition, large, interconnected slightly Cr-enriched structures with dendritic-like morphology are visible traversing the matrix, Fig. A4. These features may be interpreted as solid-state grown $ZrCr_2$ colonies that developed along fast Cr diffusion paths, such as grain boundaries or defect-rich zones, due to anisotropic growth kinetics during cooling. The absence of melting, consistent with the sub-eutectic treatment temperature, confirms a fully solid-state precipitation process.

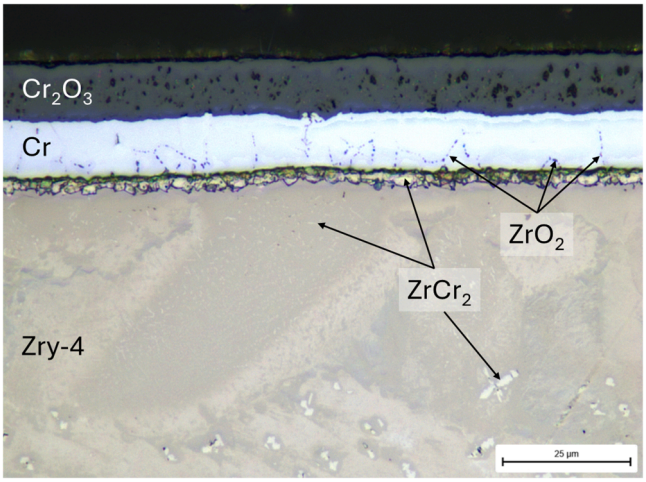

Fig. A2. High-magnification optical micrograph of the 20-µm sample after 1 hour oxidation at 1200 °C.

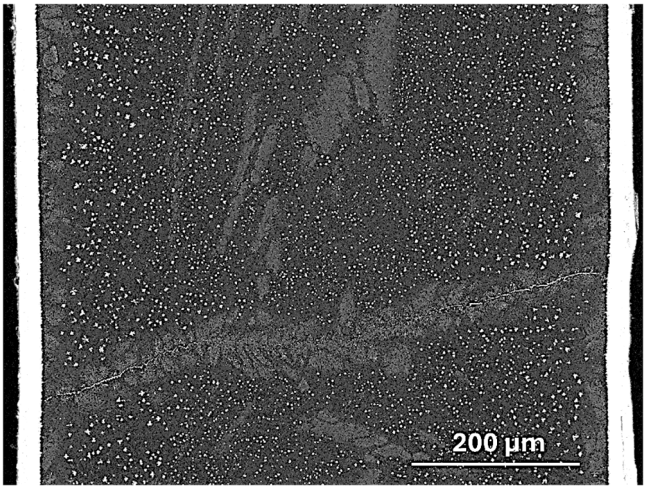

Fig. A3. High-contrast EDS Cr map of the 20-µm sample cross section after 1 hour oxidation at 1200 °C.

EDS maps of the 10-µm sample after the oxidation test at 1300 °C including analysis of Sn

Fig. A4 provides the EDS maps of Cr, Zr, Sn, and the combined color map including Cr, Zr, and O. At first glance, the superficial chromia layer and the underlying zirconia layer are visible. The remaining Zircaloy substrate is divided into two parts. Externally, elongated, needle-shaped crystals are visible, whereas in the central third of the Zry substrate finer Cr-enriched structures with dendritic-like morphology are observed similar to Fig. A3. It is assumed that the larger $ZrCr_2$ structures are formed at temperature during phase transition from β-Zr with high Cr solubility to the oxygen-stabilized α-Zr(O) with much lower Cr solubility. The significantly smaller Cr-rich precipitates in the remaining central β-Zr phase should have formed during fast cooling as described above.

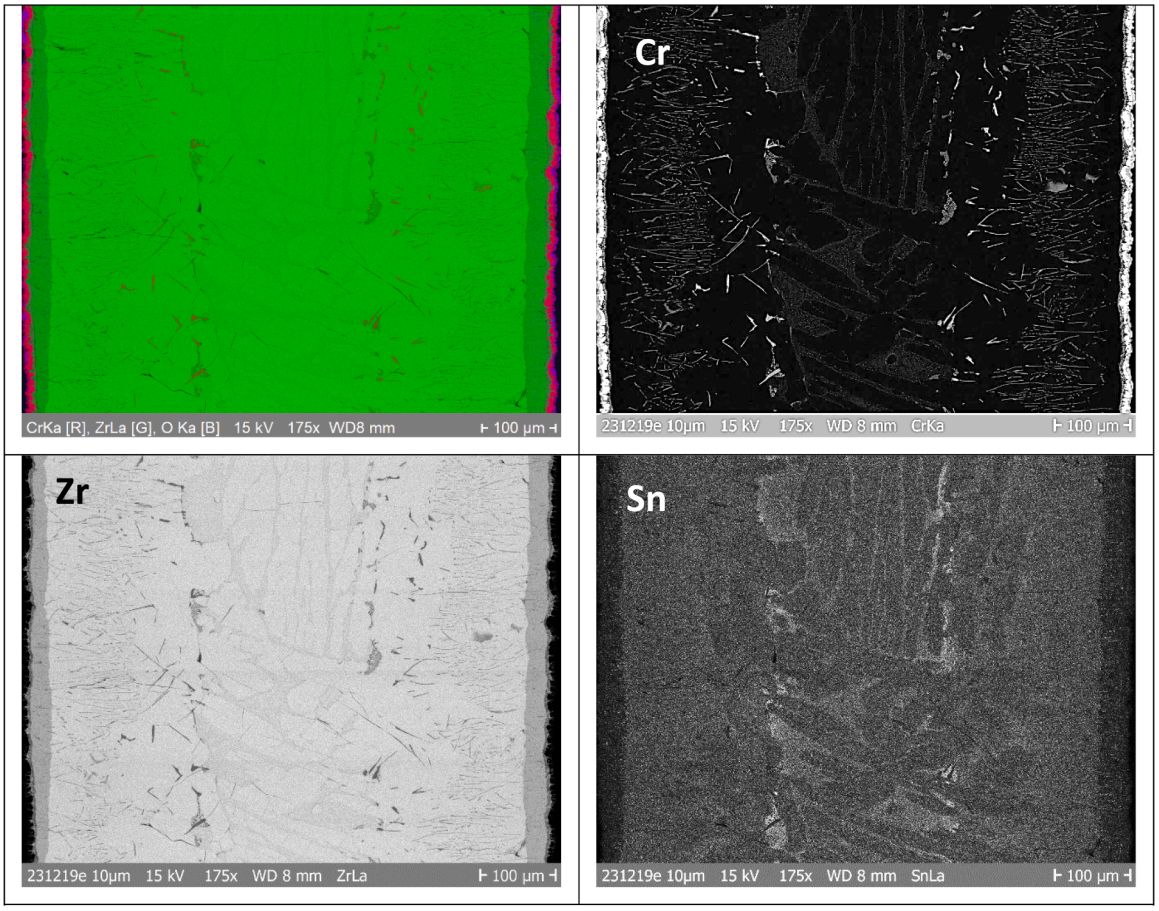

Fig. A4. EDS maps (color, Cr, Zr, Sn) of the 10-µm sample cross section after 30 min oxidation at 1300 °C.

Tin (Sn) distribution is also provided in Fig. A4. In cross-sectional micrographs of Cr-coated Zircaloy-4 oxidized at high temperature, Sn enrichment is observed in the sample interior together with Cr. This correspondence could arise because both elements exhibit similar solubility behavior in α-Zr and are rejected from the near-surface region during oxidation. While Cr diffuses inward rapidly from the coating, Sn redistributes more slowly and tends to accumulate at the advancing Cr diffusion front. Upon cooling, both elements exceed their solubility limits and co-precipitate, frequently forming mixed $Zr(Cr,Sn)_2$ intermetallics. As a result, the mid-thickness region of the bulk acts as a segregation zone where Cr and Sn enrichment coincide.

EDS maps of the 10-µm sample after the oxidation test at 1400 °C including analysis of Sn

Fig. A5 shows EDS maps of Cr, Zr, Sn, and the color maps combining Cr, Cr, and O. Relatively thin chromia layers (5 µm) are seen at the sample surface followed by thick zirconia layers. In the middle of the ZrO_2, enrichment of tin is seen. This so-called "tin line" in oxidized Zircaloy forms because tin, which is soluble in the Zr metal but has very low solubility in ZrO_2, is rejected from the oxide as it grows. During high-temperature oxidation, Sn segregates at the advancing metal/oxide interface. As the oxide thickens, this Sn-enriched interface becomes buried within the scale, appearing as a sharp mid-layer "tin line".

The remaining metallic phase in the middle of the sample seems to be mainly oxygen-stabilized α-Zr(O) with Cr enrichment in the very middle. According to the non-regular shape of these regions, they seem to be formerly molten areas. A less significant enrichment in Sn is also observed in the middle of the metallic zone, here not correlating with the Cr-enriched areas as seen after the tests at 1300 °C.

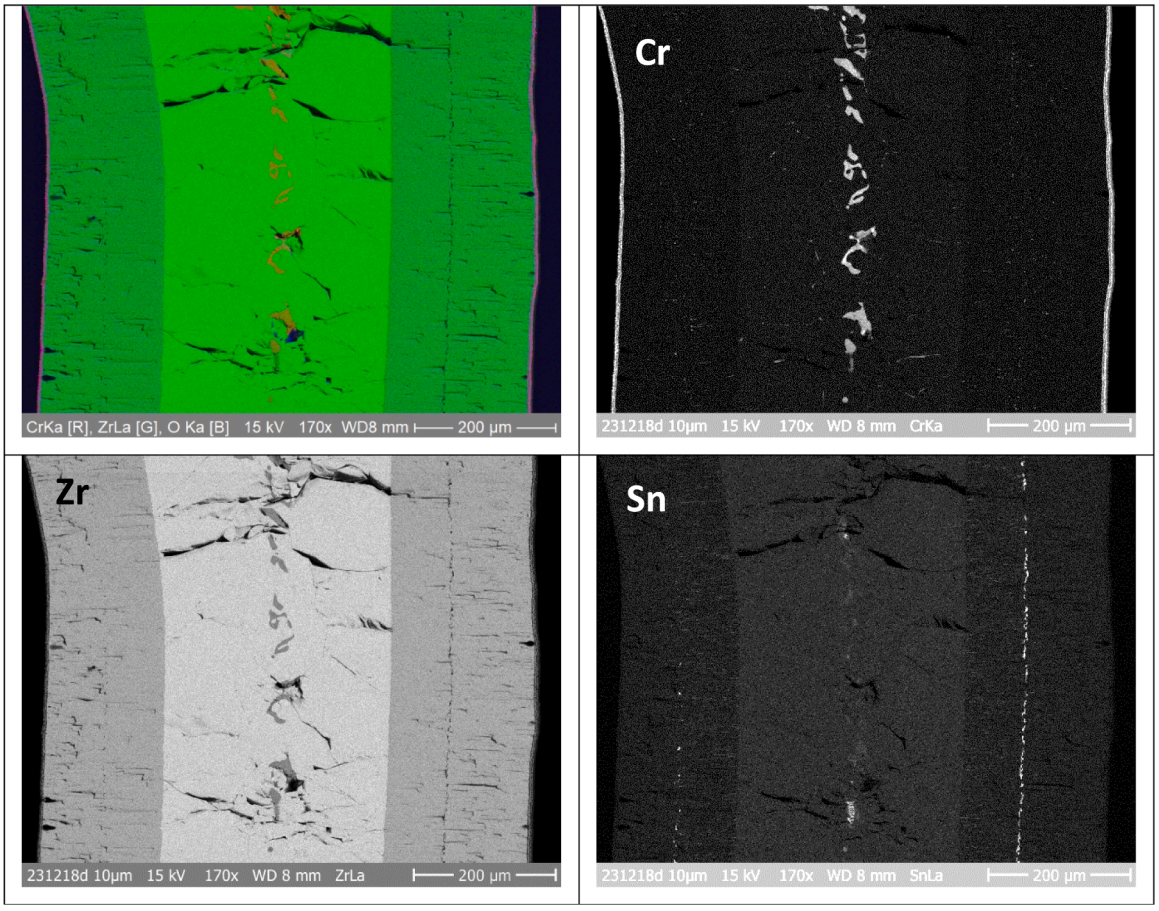

Fig. A5. EDS maps (color, Cr, Zr, Sn) of the 10-µm sample cross section after 10 min oxidation at 1400 °C.

EDS maps of the 10-µm sample after the transient oxidation test up to 1500 °C including analysis of Sn

The post-test status of the 10-µm sample after the transient test up to 1500 °C shown in the EDS maps of Fig. A6 looks similar to the same sample type after the isothermal test at 1400 °C, i.e. also above eutectic temperature. The Cr_2O_3 layer is significantly thicker (15 µm), which should be related to the considerable oxidation of the chromium coating before the eutectic temperature was reached. The average ZrO_2 scale thickness is slightly higher (226 vs. 198 µm) than after the isothermal test at 1400 °C due to the overall longer oxidation time at high temperatures. It also shows the "tin line" in the middle parts. Formerly molten Cr-rich areas as well as tin enrichment are found in the middle of the sample cross section.

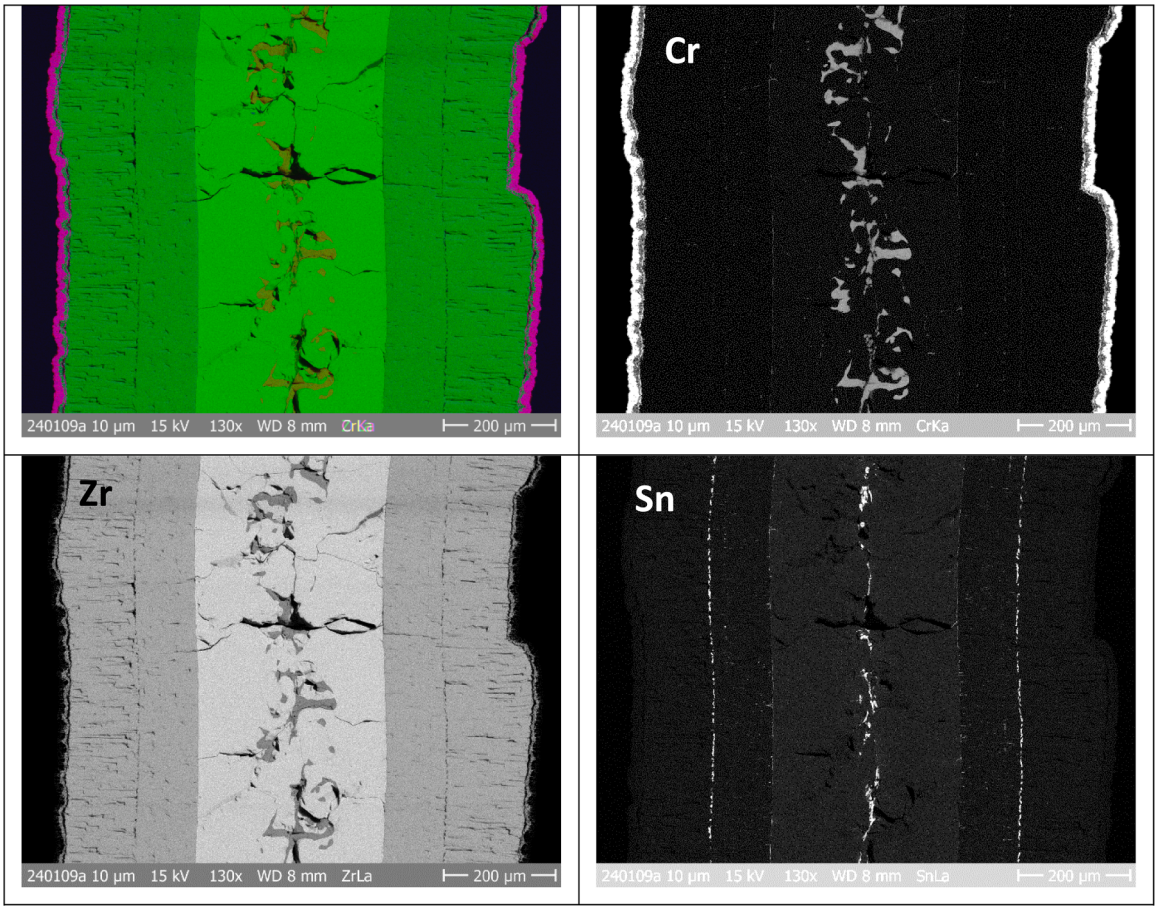

Fig. A6. EDS maps (color, Cr, Zr, Sn) of the 10-µm sample cross section after transient oxidation from 500 °C up to 1500 °C.

Appendix 2. Discussion of the edge effect

The OM cross section overview images taken after the test series below the eutectic temperature (Fig. 6, Fig. 10, and Fig. 15) show distinct edge effects, i.e. the formation of zirconia and oxygen-stabilized α-Zr(O) at the sample ends with poorly coated edges and locations of geometric singularities. These contributed to mass gain and hydrogen release and may have also affected the transition times from protective to non-protective coatings as determined from the online mass gain curves.

A first attempt was made to correct the final mass gain values by the contribution of this "disturbing" ZrO_2 formed at the edges of the samples with the following procedure. The area of zirconia at the edges was determined using the ImageJ software (version 1.54 g) and converted into ZrO_2vol/mass considering a homogenous effect along all edges of the sample. The mass gain due to the formation of zirconia at the edges was calculated based on the oxygen mass in ZrO_2 and subtracted from the measured final mass gain. The corrected data are scattering for the experiments at 1000 °C, even with a negative value for the 25-µm sample. The relative effect of the edge oxidation is high because of the only slight oxidation of the Cr coating at 1000 °C as seen in the mass gain diagrams (Fig. 4). The edge effects should have influenced the transition times for which the post-test analyses showed a fully protective effect of the coatings with 10–25 µm coating. The corrected results for the tests at 1200 °C and 1300 °C look more reasonable with mass gain values $\Delta m(5\ \mu m) >> \Delta m(10\ \mu m) > \Delta m(15,20,25\ \mu m)$, which corresponds to the results of the post-test analyses, see left column of colored lines in Fig. A7.

A second correction was done based on the post-test thicknesses of chromia, zirconia, and oxygen-stabilized α-Zr(O). The results shown by the right column of colored lines in Fig. A7 and the mass gain diagrams (Fig. 4, Fig. 8, Fig. 13) are comparable to the first correction procedure with less scatter and more accuracy. At 1000 °C, the corrected mass gains are very similar for all coating thicknesses, and at the higher temperatures there is a clear trend of an almost non-protective 5-µm coating, a partially protective 10-µm coating and protective coating of 15, 20, and 25 µm thick coatings.

These simplified analyses consider only the post-test status of the samples but not the in-situ mass gain (H_2 release) during the oxidation. Such analyses are planned in future studies using these data for validation of Cr coating oxidation and degradation models as the ECrR model of Brachet [30] and the comprehensive modelling approaches by Kim [25] and Wang [26].

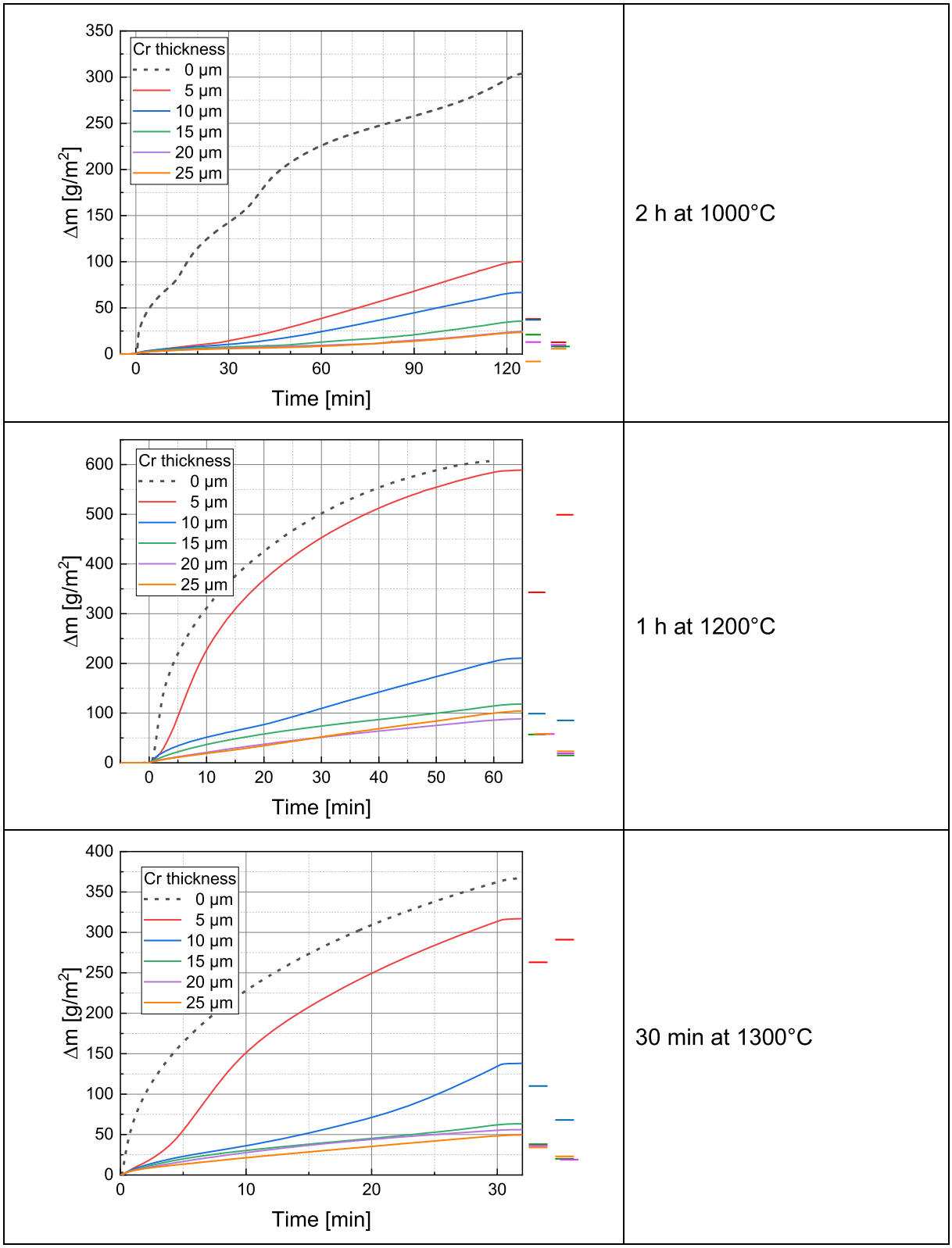

Fig. A7. Mass gain curves with corrected final mass gains. The left lines are based on the correction of the edge effect based on image analyses of the sample cross sections (Fig. 6, Fig. 10, and Fig. 15). The right lines are based on oxide (Cr_2O_3, ZrO_2) and α-Zr(O) thickness measured in OM and SEM/EDS images.

Data availability

Data will be made available on request.

References

[1] S. Zinkle, K. Terrani, J. Gehin, L. Ott, L. Snead, Accident tolerant fuels for LWRs: A perspective, J. Nucl. Mater. 448 (2014) 374–379.

[2] K. Terrani, Accident tolerant fuel cladding development: promise, status, and challenges, J. Nucl. Mater. 501 (2018) 13–30.
[3] NEA, State-of-the-art report on light water reactor accident-tolerant fuels, Nucl. Sci. (2018).
[4] C. Tang, M. Stueber, H. Seifert, M. Steinbrueck, Protective coatings on zirconium-based alloys as accident-tolerant fuel (ATF) claddings, Corros. Rev. 35 (2017) 141–165.
[5] R. Rebak, Improved and innovative accident-tolerant nuclear fuel materials considered for retrofitting light water reactors - A review, Corros. Mater. Degrad. 4 (2023) 466–487.
[6] M. Steinbrueck, N. Waeckel, A. Jasiulevicius, Accident tolerant fuel: an update report, Adv. Nucl. Technol. Int. Mölnycke Swed. (2024).
[7] J. Yang, M. Steinbrück, C. Tang, M. Große, J. Liu, J. Zhang, D. Yun, S. Wang, Review on chromium coated zirconium alloy accident tolerant fuel cladding, J. Alloys. Compd. 895 (2022) 162450 art. no.
[8] M. Steinbrueck, M. Grosse, C. Tang, J. Stuckert, H. Seifert, An overview of mechanisms of the degradation of promising ATF cladding materials during oxidation at high temperatures, High Temp. Corros. Mater. 101 (2024) 621–647.
[9] N. Vioujard, PROtect: the E-ATF solution by Framatome – overview of recent achievements and next steps, in: The 2023 Water Reactor Fuel Performance Meeting (WRFPM2023), Xi'an, China, 2023.
[10] Z. Karoutas, K. Metzger, E. Pitruzella, C. Vallencour, E. Lahoda, A. Jaworski, A. Parsi, M. Anness, C. Haas, M. Limbäck, J. Wright, Westinghouse EnCore®accident tolerant fuel and high energy program, in: TopFuel2022, Raleigh, NC, USA, 2022.
[11] U.S.NRC, Accident tolerant fuel regulatory activities - lead test assemblies [Online]. Available: https://www.nrc.gov/reactors/power/atf/lead-test.html, 2023 [Accessed July 2023].
[12] J.-C. Brachet, I. Idarraga-Trujillo, M. Flem, M. Saux, V. Vandenberghe, S. Urvoy, E. Rouesne, T. Guilbert, C. Toffolon-Masclet, M. Tupin, C. Phalippou, F. Lomello, F. Schuster, A. Billard, G. Velisa, C. Ducros, F. Sanchette, Early studies on Cr-Coated Zircaloy-4 as enhanced accident tolerant nuclear fuel claddings for light water reactors, J. Nucl. Mater. 517 (2019) 268–285.
[13] H. Yeom, B. Maier, G. Johnson, T. Dabney, M. Lenling, K. Sridharan, High temperature oxidation and microstructural evolution of cold spray chromium coatings on Zircaloy-4 in steam environments, J. Nucl. Mater. 526 (2019) 151737 art. no.
[14] J.-C. Brachet, E. Rouesne, J. Ribis, T. Guilbert, S. Urvoy, G. Nony, C. Toffolon-Masclet, M.Le Saux, N. Chaabane, H. Palancher, A. David, J. Bischoff, J. Augereau, E. Pouillier, High temperature steam oxidation of chromium-coated zirconium-based alloys: kinetics and process, Corros. Sci. 167 (2020) 108537 art. no.
[15] E. Kashkarov, D. Sidelev, M. Syrtanov, C. Tang, M. Steinbrück, Oxidation kinetics of Cr-coated zirconium alloy: effect of coating thickness and microstructure, Corros. Sci. 175 (2020) 108883 art. no.
[16] D. Kim, M. Steinbrück, M. Grosse, C. Tang, Y. Lee, Eutectic reaction and oxidation behavior of Cr-coated Zircaloy-4 accident-tolerant fuel cladding under various heating rates, J. Nucl. Mater. 583 (2023) 154538 art. no.
[17] J. Yang, T.C.U. Stegmaier, M. Steinbrück, W.S.M. Große, H. Seifert, High temperature Cr-Zr interaction of two types of Cr-coated Zr alloys in inert gas environment, J. Nucl. Mater. 547 (2021) 152806 art. no.
[18] J. Liu, M. Steinbrück, M. Große, U. Stegmaier, C. Tang, D. Yun, J. Yang, Y. Cui, H. Seifert, Systematic investigations on the coating degradation mechanism during the steam oxidation of Cr-coated Zry-4 at 1200°C, Corros. Sci. 202 (2022) 110310 art. no.
[19] J. Liu, C. Tang, M. Steinbrück, J. Yang, U. Stegmaier, M. Große, D. Yun, H. Seifert, Transient experiments on oxidation and degradation of Cr-coated Zircaloy in steam up to 1600°C, Corros. Sci. 192 (2021) 109805 art. no.
[20] D. Arias, J. Abriata, The Cr-Zr (Chromium-Zirconium) system, Bull. Alloy Ph. Diagr. 7 (1986) 237–244.
[21] J.-C. Brachet, T. Guilbert, D. Hamon, N. Guillaume, P. Gokelaere, A new "ECR" parameter to support high-temperature steam oxidation behavior of Cr-coated Zr-based E-ATF cladding, in relation with their post-quenching mechanical strength and ductility (for LOCA and slightly beyond conditions), in: TopFuel, Grenoble, France, 2024.
[22] X. Han, J. Xue, S. Peng, H. Zhang, An interesting oxidation phenomenon of Cr coatings on zry-4 substrates in high temperature steam environment, Corros. Sci. 156 (2019) 117–124.
[23] M. Steinbrück, U. Stegmaier, M. Große, L. Czerniak, E. Lahoda, R. Daum, K. Yueh, High-temperature oxidation and quenching of chromium-coated zirconium alloy ATF cladding tubes with and w/o pre-damage, J. Nucl. Mater. (2022) 153470 art. no.
[24] Y. Xiang, H. Yang, Q. Chen, X. Peng, R. Zhang, T. Wei, C. Liu, H. Chen, Long-term high-temperature steam oxidation behavior of Cr-coated Zircaloy-4 alloy for accident tolerant fuel, Mater. Corros. 73 (2022) 2009–2018.
[25] D. Kim, Y. Lee, Mechanisms of steam oxidation-induced degradation of chromium coating on zirconium alloys at high temperatures, Corros. Sci. 254 (2025) 113055 art. no.
[26] D. Wang, S.L.K. Wu, Y. Zhang, G. Su, X. Liu, High-temperature oxidation of accident tolerant Cr-coated Zr alloy cladding: model development and validation, J. Nucl. Mater. 606 (2025) 155621 art. no.
[27] M. Steinbrück, Prototypical experiments relating to air oxidation of Zircaloy-4 at high temperatures, J. Nucl. Mater. 392 (2009) 531–544.
[28] J. Baek, Y. Jeong, Breakaway phenomenon of Zr-based alloys during a high-temperature oxidation, J. Nucl. Mater. 372 (2008) 152–159.
[29] M. Steinbrück, N. Vér, M. Grosse, Oxidation of advanced zirconium cladding alloys in steam at temperatures in the range of 600-1200°C, Oxid. Met. 76 (2011) 215–232.
[30] J.-C. Brachet, T. Guilbert, S. Urvoy, E. Rouesne, M. Peyret, T. Vandenberghe, C. Prou, T. Le-Hong, D. Hamon, Some practical methodologies to assess the overall high temperature (one-sided) steam oxidation protectiveness of chromium-based coatings on a zirconium-based substrate, as enhanced – Accident tolerant (Nuclear) fuels (E-ATF) claddings, J. Nucl. Mater. 606 (2025) 155620 art. no.
[31] D.J. Young, High Temperature Oxidation and Corrosion of Metals, Elsevier Ltd., 2016.
[32] J. Deng, J. Zuo, D. Geng, Q. Sun, Z. Song, J.R. Sun, Temperature-time dependence and mechanisms of redox reaction in Cr-coated Zr alloy cladding during steam oxidation at 900–1250 °C, J. Nucl. Mater. 596 (2024) 155094 art. no.
[33] G. Schanz, B. Adroguer, A. Volchek, Advanced treatment of zircaloy cladding high-temperature oxidation in severe accident code calculations part I. Experimental database and basic modeling, Nucl. Eng. Des. 232 (2004) 75–84.
[34] J. Brachet, (2026) "Application of the new ECrR criterion to KIT experimental results (working title)". *to be published in JNM*.
[35] S. Wu, X. Wu, Y. Zhang, D. Wang, P. Ma, W. Tian, S. Qiu, G. Su, Study on eutectic melting and high-temperature oxidation characteristics of Cr coated Zr alloy cladding under steam atmosphere at 1400–1500°C, J. Alloys. Compd. 1039 (2025) 183389 art. no.
[36] D. Wang, R. Zhong, X. Wu, Y. Zhang, X. Li, J. Yu, L. Y, G. Su, S. Qiu, W. Tian, Y. Liao, Z. Peng, C. Guo, Z. Song, J. Sun, Study on eutectic-oxidation coupling reaction of Cr-Zr system in high temperature steam environment, J. Nucl. Mater. 596 (2024) 155082 art. no.
[37] Y. Ohishi, T. Kondo, T. Ishikawa, J. Okada, Y. Watanabe, H. Muta, K. Kurosaki, S. Yamanaka, Physical properties of molten core materials: Zr-Ni and Zr-Cr alloys measured by electrostatic levitation, J. Nucl. Mater. 485 (2017) 129–136.
[38] B. Kweon, H. Yook, D. Kim, Y. Lee, Assessment of the impact of Zr-Cr eutectic reaction on the structural integrity of Cr-coated ATF cladding, J. Nucl. Mater. 617 (2025) 156166 art. no.
[39] H. Okamoto, O-Zr (Oxygen-Zirconium), J. Ph. Equilibria Diffus. 28 (2007) 498.
[40] M. Steinbrueck, in: Proceedings of the 30th International QUENCH Workshop, Karlsruhe, Germany, 2026.